The Report Committee for Ithza Montserrat Lopez Aguilar

certifies that this is the approved version of the following report:

Integrated Magnetic Localization Sensing and Actuation of Steerable Robotic Catheter for Peripheral Arterial Disease Treatment

APPROVED BY

SUPERVISING COMMITTEE:

Lei Zhou, Supervisor

Mitchell Pryor

Integrated Magnetic Localization Sensing and Actuation of Steerable Robotic Catheter for Peripheral Arterial Disease Treatment

by

Ithza Montserrat Lopez Aguilar

Report

Presented to the Faculty of the Graduate School of

The University of Texas at Austin

in Partial Fulfillment

of the Requirements

for the Degree of

Master of Science in Engineering

The University of Texas at Austin

December 2023

To my family, friends, and educators

Acknowledgments

I would like to thank my supervisor, Dr. Lei Zhou, for her continuous support and valuable guidance throughout my graduate school journey. Secondly, I would like to thank Dr. Mitchell Pryor for his mentorship and support on my last semester. From the Precision Mechatronics and Control Lab, I would like to thank Jungjie Wu for his mentorship in the development of the project. Sections 3.2-3.5, and 5.1-5.2 are based from our collaborated work in:

J. Wu *et al.*, "Integrated Magnetic Location Sensing and Actuation of Steerable Robotic Catheters for Peripheral Arterial Disease Treatment," in *IEEE Robotics and Automation Letters*, vol. 8, no. 9, pp. 5656-5663, Sept. 2023, doi: 10.1109/LRA.2023.3295297.

Finally, I would like to thank my family and friends for always believing in me.

Ithza Montserrat Lopez Aguilar

The University of Texas at Austin

December 2023

Abstract

Integrated Magnetic Localization Sensing and Actuation of Steerable Robotic Catheter for Peripheral Arterial Disease Treatment

Ithza Montserrat Lopez Aguilar, M.S.E

The University of Texas at Austin, 2023

Supervisor: Lei Zhou

Magnetically Steerable Robotic Catheters (MSRC) exhibit potential in treating Peripheral Arterial Diseases (PAD) through the precise steering of a catheter tip via magnetic actuation. PAD, characterized by the narrowing of blood vessels, affects approximately 6.5 million people age 40 and older in the US, necessitating effective treatment options. Percutaneous Endovascular Intervention (PEI) is the conventional approach but often lacks efficient navigation through intricate vasculatures. Existing MSRC systems rely on continuous fluoroscopic imaging for real-time location sensing, posing radiation risks to patients and medical staff. To reduce x-ray

radiation exposure, this study presents an innovative MSRC system that integrates magnetic location sensing and actuation. The catheter features a magnetic tip for external electromagnetic steering and uses a cylindrical array of magnetic sensors for real-time location estimation. A mathematical model for magnetic localization is presented, with real-time application using the Levenberg-Marquardt algorithm. The integration of magnetic steering and sensing is showcased through real-time navigation experiments. The system components, including the magnet, catheter design, feeding mechanism, sensor array, and Helmholtz coils, are detailed. Experimental results using a prototype MSRC demonstrate an average position estimation error of 0.95 mm after calibration. The system successfully navigates vascular phantoms using actuated magnetic steering and sensing, highlighting its potential to minimize x-ray exposure during PAD surgeries.

Table of Contents

List of Tables

List of Figures

Chapter 1

Introduction

1.1 Motivation

The United States Centers for Disease Control and Prevention reported a significant prevalence of Peripheral Arterial Disease (PAD) among individuals aged 40 and above, with approximately 6.5 million cases in the US [3]. PAD is a medical condition characterized by the narrowing or blockage of blood vessels in the lower extremities, resulting in debilitating symptoms such as pain, limited mobility, intermittent claudication, and, in severe cases, critical limb ischemia [4]. The conventional treatment for PAD involves percutaneous endovascular intervention (PEI) [5], which includes the insertion of a catheter into the affected blood vessels through a femoral artery incision, guided by fluoroscopic imaging, with the goal of deploying a balloon or stent to restore normal blood flow.

To enhance the existing workflow, extensive research and development efforts have explored steerable robotic catheters [6, 7]. Magnetically steerable robotic catheters (MSRCs) have gained increasing attention due to their inherent advantages, such as enabling robotic-assisted navigation [8]. They also allow the use of

compact and ultra-thin catheters [9, 10, 11], eliminating the need for embedded steering mechanisms like tendons and offering contactless force and torque transmission [12].

In contemporary PEI procedures, catheters often lack active steering capabilities at their distal ends, rendering them passive and unsuitable for efficient navigation through intricate leg vasculatures characterized by bifurcations and irregular branches. As a result, operating these passive catheters becomes exceedingly demanding and time-consuming [5].

1.2 Overview

This report details the mathematical modeling, design, and experimental assessment of a Magnetically Steerable Robotic Catheter, with the aim of its application in the context of PAD. The following section provides a concise summary of the principal tasks and outcomes.

Chapter 2

PAD is a condition characterized by the narrowing of blood vessels due to plaque accumulation within artery walls as depicted in Figure 2.1. The prevalence of PAD is higher in adults aged 40 and above, with an increased risk for diabetics, among whom one out of three individuals over the age of 50 is affected by PAD.

During angioplasty, a catheter is inserted through a small incision in the upper leg, and a dye is injected to visualize blood flow. The patient remains awake, although some anesthesia is provided for pain relief. The procedure typically lasts one to three hours, and in some cases, patients may need to spend the night at the hospital. The use of fluoroscopy in the procedure exposes patients and healthcare

professionals to radiation.

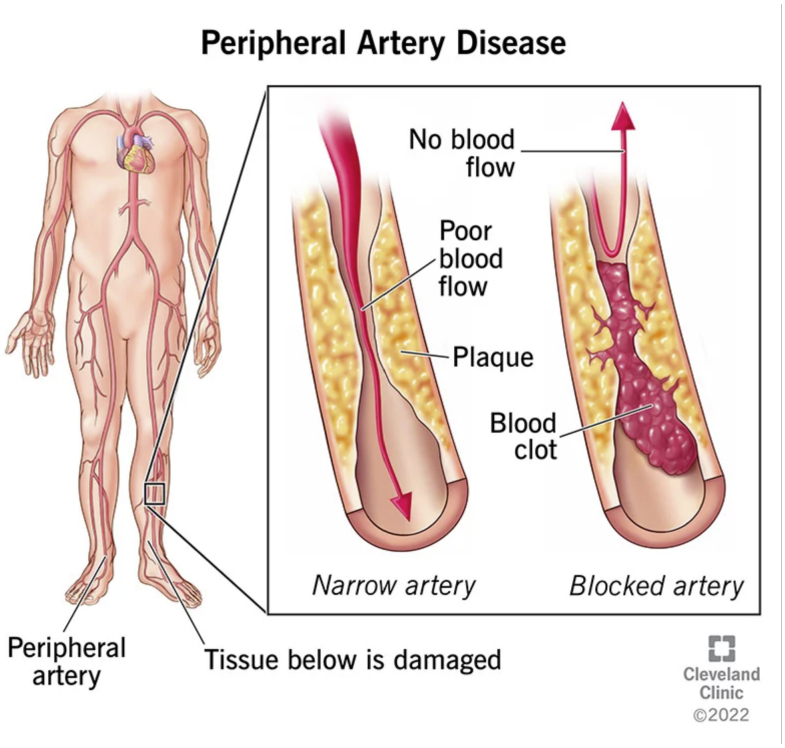

Figure 2.1: Peripheral Arterial Disease described as plaque buildup in arteries obstructing blood flow, adapted from [1]

Magnetic localization has demonstrated effectiveness in applications such as industrial robot calibration, robotic capsule endoscopes, miniature robots, and continuum manipulators. Small permanent magnets were found to exhibit size-dependent magnetic properties, which have significant implications for designing sensors for long-range magnetic detection. However, when applying magnetic localization to Magnetically Steerable Robotic Catheter (MSRC) systems for PAD interventions, several technical challenges were identified, including the need for highly sensitive sensors and noise reduction algorithms to accommodate the smaller diameter of the catheter, the development of innovative calibration algorithms, and addressing the saturation of magnetic sensors by actuation fields.

Chapter 3

The MSRC, as illustrated in Figure 3.1, features a sensor array with four sensors on each side of its cylindrical structure, resulting in four cascading arrays for comprehensive coverage. Helmholtz coils situated on the posterior leg induced a current, allowing the magnet to tilt and reorient itself effectively to navigate arterial bifurcations during PAD treatment.

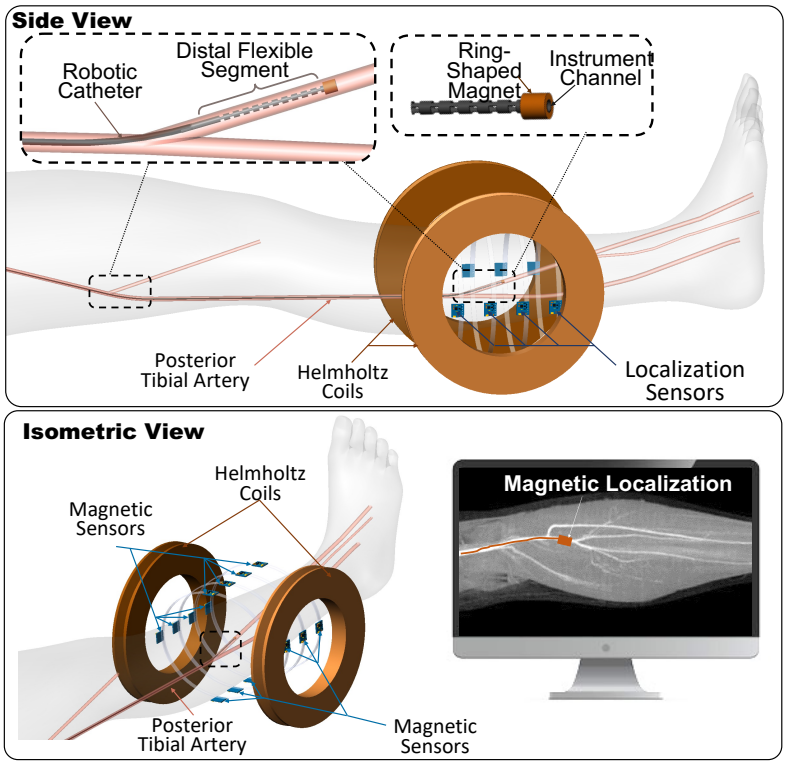

Figure 3.1: Conceptual illustration of a magnetically steerable robotic catheter (MSRC) with magnetic localization for peripheral arterial disease (PAD) treatment to reduce x-ray radiation.

A mathematical model for the magnetic localization algorithm was developed, which considered the magnetic flux density at sensor locations based on a

dipole model. The estimation of the magnet's position and orientation was achieved through a nonlinear optimization problem, using the Levenberg-Marquardt (LM) algorithm for real-time application.

The actuation implementation involved determining the angle of tilt by varying the current levels on the MSRC. This angle-duty cycle relationship was utilized to introduce actuation tracking into the navigation process, enabling precise catheter steering. The results demonstrated a linear relationship between angle and duty cycle as seen in Figure 3.5

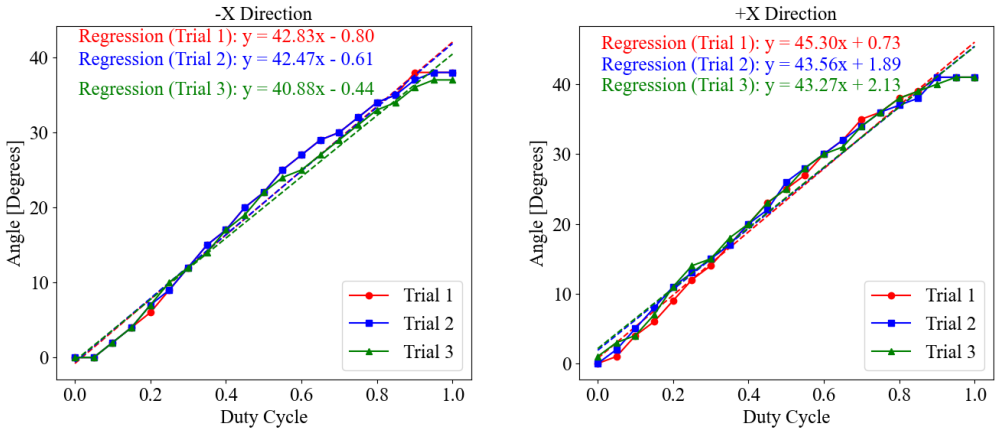

Figure 3.5: Data testing MSRC steering angle at various duty cycles to both directions and their calculated linear regressions. a) Testing for $-\mathbf{x}$ direction steering b) Testing for $+\mathbf{x}$ direction steering

Chapter 4

The system comprised a magnetic tip, a flexible catheter distal segment, a catheter feeding mechanism, a magnetic sensor array, Helmholtz coils for steering,

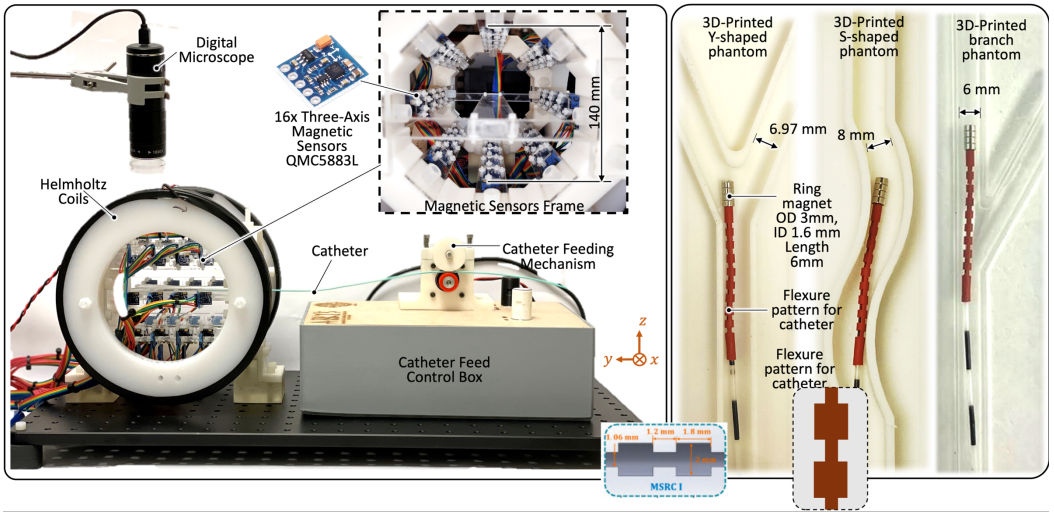

Figure 4.1: Photograph of the magnetically steerable robotic catheter prototype and subsystems.

and three distinct vasculature models as depicted in Figure 4.1. The magnet section detailed the use of axially magnetized permanent magnets placed at the catheter's distal end, aiming to enable magnetically-guided navigation within blood vessels. The catheter design took into account the geometry of posterior arteries and bifurcations, ensuring it met anatomical constraints and could navigate through arteries less than 4 mm in diameter. The flexible catheter distal was created to provide the necessary flexibility for efficient steering within the vasculature. A feeding mechanism, employing a friction drive system, was used to facilitate catheter insertion. Magnetic sensors were positioned in a cylindrical array around the catheter's tip to provide real-time localization information. Additionally, Helmholtz coils were used for magnetic steering.

Three distinct vasculature models were created for testing the MSRC's maneuverability, including models with S-curved paths and bifurcations, which allowed the evaluation of real-time accuracy and actuation capabilities.

Table 5.1: Average localization error with and without calibrations.

Data Range	w/o calib.	w/ [13] calib.	w/ nested calib.
All (51 pts) xyz	10.16 mm	5.28 mm	4.53 mm
All (51 pts) ϕ	6.07°	3.20°	3.77°
All (51 pts) ϕ	12.48°	8.52°	8.62°
Center (27 pts) xyz	4.34 mm	1.74 mm	0.95 mm
Center (27 pts) θ	1.46°	0.98°	1.00°
Center (27 pts) ϕ	3.84°	3.08°	1.75°

Chapter 5

Calibration grids were designed to precisely position magnets in both straight and angled orientations with respect to the **y**-axis of the global frame. The calibration involved using two calibration plates with magnets placed at 51 positions. The localization results showed the estimated position of the magnet in comparison to the true position, with the magnet positions within the sensor array having smaller errors, but errors increased towards the plate's edge. The results also indicated a bias in the localization error in the **y**-axis towards the same direction as the magnet location, particularly at the ends of the plate.

Then the calibration was validated by placing magnets at angled positions on the sensor Calibration Plate 2. The improvements were quantified in localization accuracy with and without calibration, showing substantial reductions in localization errors in the central columns as seen in Table 5.1

The experiments involved catheter insertion into bifurcations with real-time tracking and navigation, detailing the navigation steps and illustrating the magnet's movements during these experiments. The experiments showcased the integration of magnetic steering and magnetic location sensing, emphasizing their effectiveness.

The final section extends the navigation experiments to incorporate actuation using the catheter motor driver as seen in Figure 5.5. The process involved actuating

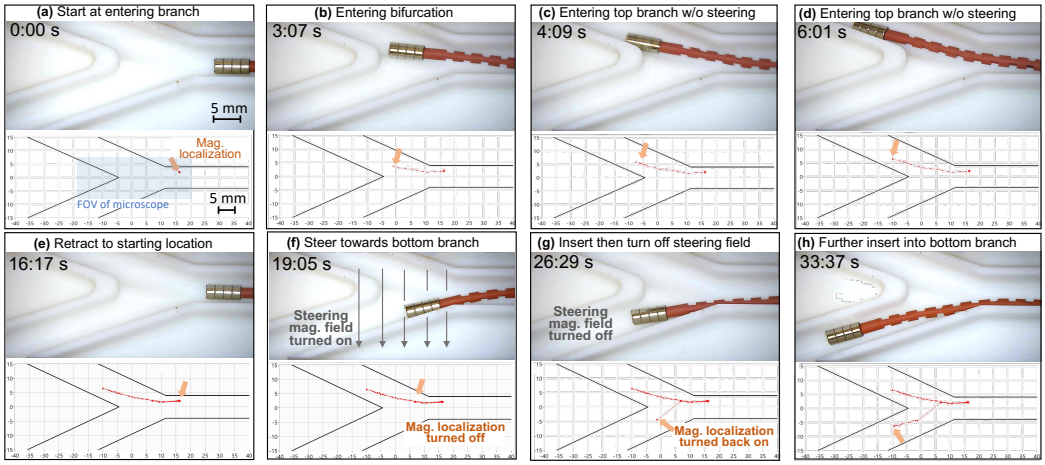

Figure 5.3: Snapshots of digital microscope video for the prototype magnetically steerable robotic catheter navigating through the 3D-printed vascular phantom with 20° bifurcation and the screenshots of the user interface showing the catheter tip location estimation using magnetic localization.

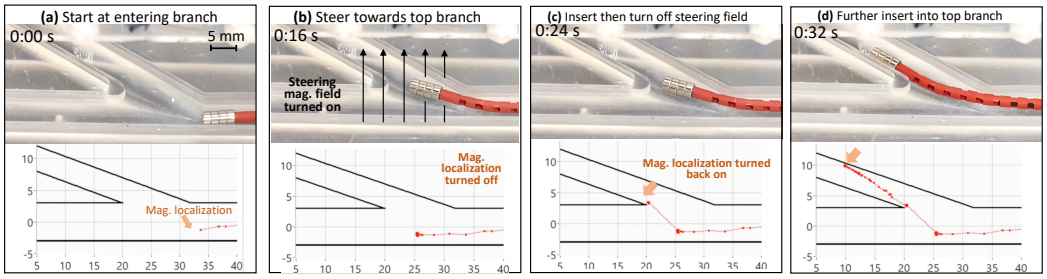

Figure 5.4: Snapshots of the prototype magnetically steerable robotic catheter navigating through the 3D-printed vascular phantom with a 30°e bifurcation.

the catheter while simultaneously tracking the magnet's location. The accuracy on the **y**-axis was increased by adding more columns to the calibration plate for sensor localization and calibration.

The integration of sensing and actuation was realized through the implementation of key equations, enhancing the catheter's control during navigation as seen in Figure 5.5. These experiments offered valuable insights into the potential for improved accuracy and control in future MSRC applications.

Chapter 6

The navigation simulations have successfully demonstrated the MSRC's feasibility in surgical procedures for treating PAD. Building upon this foundation, future work will emphasize improving the calibration of sensor localization to achieve higher precision, allowing for three-dimensional actuation and sensing to expand the MSRC's capabilities across the **XYZ** axis. These advancements are expected to propel the application of MSRC technology in minimally invasive surgical interventions, offering benefits in precision and efficiency. The forthcoming sections will delve into these future research directions, providing detailed insights into their potential implications and contributions to the field of medical robotics and intervascular procedures.

The current calibration algorithm successfully considers sensor translational positions and magnetic strength. However, future work should explore the inclusion of sensor orientation in the calibration process to enhance the overall accuracy of the magnetic localization system. Furthermore, the research will focus on the coupled optimization of sensor location, orientation, and magnet properties. Additionally, future calibration efforts may introduce weighted adjustments for center-range magnet positions, particularly those situated close to their nominal locations. This approach can offer a more nuanced calibration process, optimizing critical regions within the sensor array to improve system accuracy and reliability.

The existing catheter system has limitations concerning the maximum turning angle, currently capped at 40°. To enhance the catheter's maneuverability in navigating complex artery geometries, investigation and testing of various flexure patterns will be continued. Additionally, exploring alterations to the material used

in the catheter's distal segment could further enhance flexibility, enabling more substantial turns.

The current system facilitates catheter movement in the **XY** plane, whereas biological vasculatures exhibit motion in the **XYZ** space. To model more accurate catheter traversal through the body's vasculatures, achieving **XYZ** motion is imperative. This will involve expanding the data points along the **XYZ** axes, extending the grid plates used in previous experiments, and incorporating the full **XYZ** motion range. Additionally, to enable effective actuation along the **z**-axis, an additional set of Helmholtz coils will be implemented. These coils will offer actuation capabilities both upwards and downwards, allowing the catheter system to navigate not only laterally within the **XY** plane but also incorporate vertical movement along the **z**-axis.

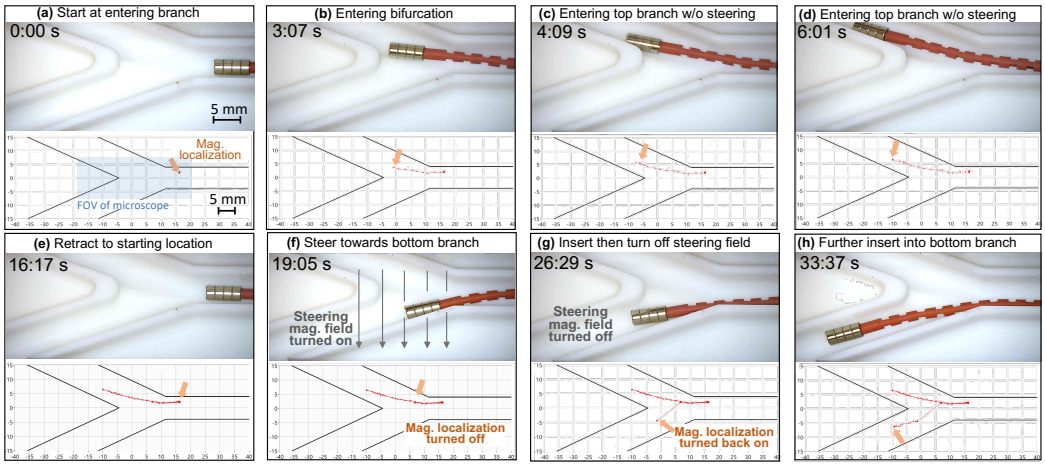

Figure 5.5: Snapshots of digital microscope video for the prototype magnetically steerable robotic catheter navigating through the 3D-printed vascular phantom with 20° bifurcation and the screenshots of the user interface showing the catheter tip location estimation using magnetic localization.

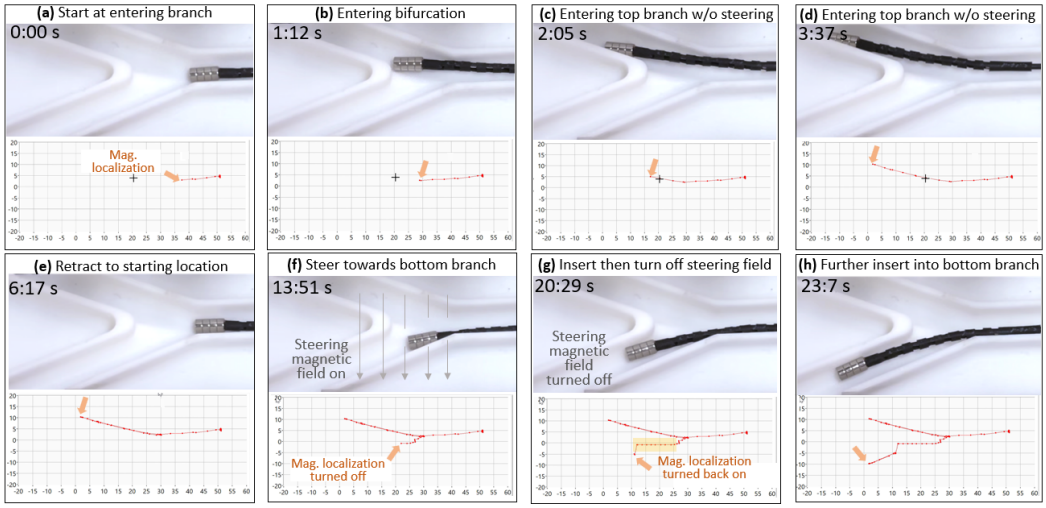

Figure 5.5: Snapshots of digital microscope video for the prototype magnetically steerable robotic catheter navigating through the 3D-printed vascular phantom with 20° bifurcation and the screenshots of the user interface showing the catheter tip location estimation using magnetic localization and tracked actuation.

Chapter 2

Literature Review

2.1 Peripheral Arterial Disease Procedure

Peripheral Arterial Disease (PAD) is a progressive narrowing of the blood vessels, often caused by the collection of plaque in the inner lining of the artery wall. The disease is most common in adults ages 40 and up, with increased risk for diabetics. One out of three diabetics over the age of 50 have PAD, and up to 70 percent of limb amputations not caused by trauma are performed on diabetics with PAD [14].

When plaque builds up in the arteries, it restricts the supply of oxygen to the heart. Angioplasty is the procedure used to open the arteries and improve blood flow by widening the blocked part of the artery [15]. The procedure is conducted through a blood vessel, where the doctor will make a small incision in the upper leg to insert a catheter into the vessel and inject a dye for blood flow visualization. The catheter is guided down the artery using fluoroscopic imaging. The patient is awake throughout the procedure. Some anesthesia is provided for pain and relaxation, but can still feel pressure and discomfort. The procedure takes one to three hours, and

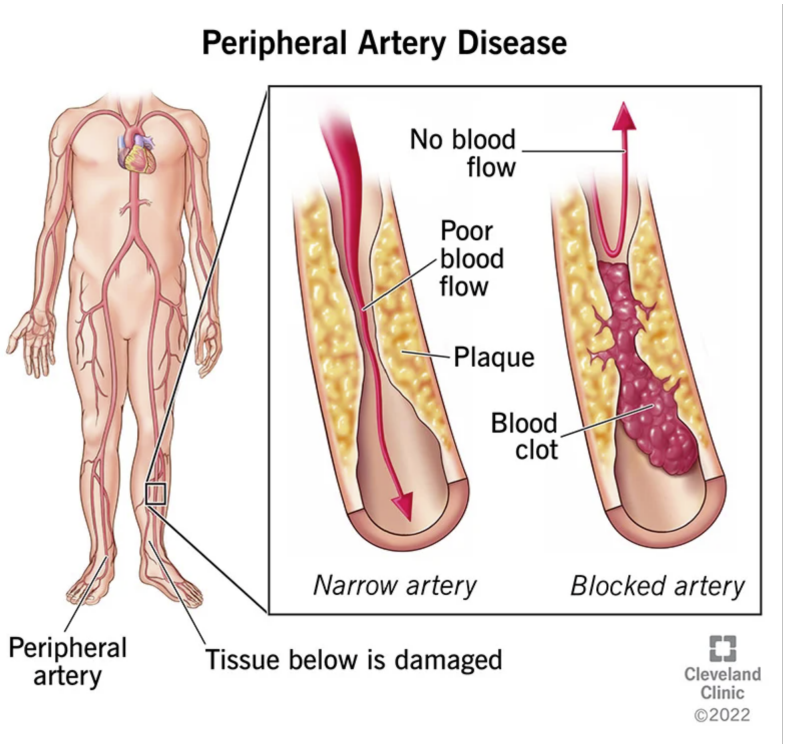

Figure 2.1: Peripheral Arterial Disease described as plaque buildup in arteries obstructing blood flow, adapted from [1]

the patient may need to spend the night at the hospital [16].

The success of fluoroscopic imaging relies heavily on the physician's manual skill and experience, introducing variability and uncertainty in the standard of care for patients [17]. Additionally, the use of fluoroscopy poses significant health risks for healthcare professionals and patients alike [18] [19]. As procedures become more complex and patients' clinical conditions worsen, longer exposure times can lead to increased X-ray radiation exposure. This radiation can potentially result in skin damage [20] and elevate the long-term risk of developing cancer [21]. Currently, even with the latest fluoroscopic equipment, interventional procedures can still expose both patients and physicians to substantial radiation doses.

2.2 Permanent Magnets

Permanent magnets are critical components in numerous technological applications, primarily due to their unique ability to generate a magnetic field that persists without the need for an external power source [22]. One of the fundamental characteristics of permanent magnets is their magnetic flux density. This property quantifies the strength of the magnetic field produced by the magnet. Properties in the flux density can be manipulated to optimize its design and functionality.

Material properties, magnet size, and shape are key elements that greatly affect the flux density of a permanent magnet. Different materials possess distinct magnetic properties, such as saturation magnetization and coercivity, which determine the maximum achievable magnetic induction. Smaller magnets often exhibit lower flux densities compared to larger ones made from the same material. This phenomenon arises from the distribution of magnetic domains within the magnet. Smaller magnets may have fewer aligned domains, leading to weaker overall magnetization and reduced flux density [23]. Engineers and designers must consider the trade-offs between magnet size and magnetic strength when choosing magnets for specific applications, especially when space is limited. The geometry of the magnet can lead to variations in the distribution of the magnetic field. Magnets with complex shapes or irregularities, such as sharp edges, may exhibit non-uniform flux densities across their surfaces [24]. Designers must carefully account for these variations when incorporating permanent magnets into devices or systems to ensure the intended magnetic field behavior.

Small permanent magnets exhibit size-dependent magnetic properties that can significantly impact their behavior. At a distance from these small magnets, sensors interact with a magnetic field characterized by a dipole pattern. Further-

more, sensors positioned far from small magnets experience a reduction in magnetic field strength, following the inverse cube law [25]. This principle has substantial implications for designing sensors intended for long-range magnetic detection.

2.3 Magnetic Localization

Magnetic localization, a technology relying on the measurement of magnetic fields emanating from either a permanent magnet (PM) or a coil to deduce its position and orientation, has exhibited remarkable performance in diverse applications. These applications span industrial robot calibration [26], robotic capsule endoscopes [27], miniature robots [28] [29], and continuum manipulators [30]. However, for magnetic localization to seamlessly integrate into MSRC's systems employed in PAD interventions, several formidable technical challenges need to be addressed.

The catheter's diameter profile must align with the vessel lumen, requiring a small diameter (3 mm or less). This is significantly smaller than the size of the PM used in previous implementations. This size difference can introduce sensor signal noise, resulting in inaccuracies in location estimation. To counter this, it is crucial to utilize highly sensitive sensors and employ noise reduction algorithms for achieving precise catheter location estimation. The sensors must meet specific requirements, including the capability to read and filter the Earth's magnetic field, which spans from 0.25 to 0.65 Gauss [31]. Consequently, the sensors must possess a resolution of at least 0.01 Gauss within the Earth's magnetic field range.

The accuracy of magnet localization hinges on the precise knowledge of sensor locations and the PM model. These are often assumed to be known prior to testing. To mitigate these uncertainties, data-driven calibration algorithms for sensor locations and PM dipole moments have been developed [13]. However, existing

calibration procedures usually address various parametric uncertainties sequentially, potentially leading to suboptimal calibration outcomes. Innovative calibration algorithms are necessary, considering the interplay between the estimation of different uncertainties to enhance magnetic localization accuracy.

MSRC systems require a robust external magnetic field to facilitate catheter steering, typically generated by actuation coils [32] [2] or a sizable PM [8]. However, these actuation fields can saturate the magnetic sensors used for localization. Recent research has explored the simultaneous magnetic actuation and localization of continuous robots [33] [34]. Still, this limitation has not been entirely resolved.

2.4 Conclusion

The current reliance on fluoroscopic imaging during PAD procedure introduces variability and radiation exposure risks. There is a need for safer, more precise technologies to reduce radiation and improve PAD interventions. Acquiring permanent magnets proves challenging due to the limited size of peripheral vasculatures. Small permanent magnets exhibit size-dependent properties that affect their magnetic behavior. The implementation of MSRC towards PAD shows the need for smaller-diameter catheters, precise sensor locations, and improved calibration procedures to enhance localization accuracy. The potential for magnetic sensor saturation due to simultaneous magnetic actuation within MSRC systems presents another issue to be resolved. In summary, the literature review identifies the pressing need for innovative solutions in PAD interventions, highlights the critical role of permanent magnets, and outlines the challenges faced in implementing magnetic localization technology in MSRC systems.

Sourcing of the magnet is limited by the geometry of the arteries. In addi-

tion to needing a small size magnet for arterial navigation, the magnet must also be hollow to accommodate elements passing through for artery dilation. The use of small magnets with distant sensors introduces noise in the data, prompting experimentation with noise filtration. The small size of the magnet and its distance from the sensors allows for the magnetic flux to be described by the dipole model. From the permanent magnet's flux density, various algorithms can be implemented and derived to describe the magnet's positions and orientation from the sensor readings. Similarly, the saturation on the sensors from activation of the coils require the development of an algorithm to track the catheter's position during actuation.

Chapter 3

Operating Principle and Modeling

3.1 Operating Principle

The sensor array was configured cylindrically, accommodating four sensors on each side of the structure. This symmetrical arrangement extended horizontally, resulting in four arrays cascading down the cylindrical surface. This layout ensured comprehensive coverage, facilitating precise monitoring and data collection from all axes of the cylindrical structure. Figure 3.1 depicts an illustration of the MSRC equipped with magnetic localization technology for the treatment of PAD.

Complementing the sensor array were the Helmholtz coils, situated on both sides of the posterior leg. These coils played a crucial role in inducing a current, enabling the magnet to tilt and reorient itself effectively for navigating arterial bifurcations during the treatment of PAD.

The Side View of Figure 3.1 depicts a ring-shaped magnet located at the

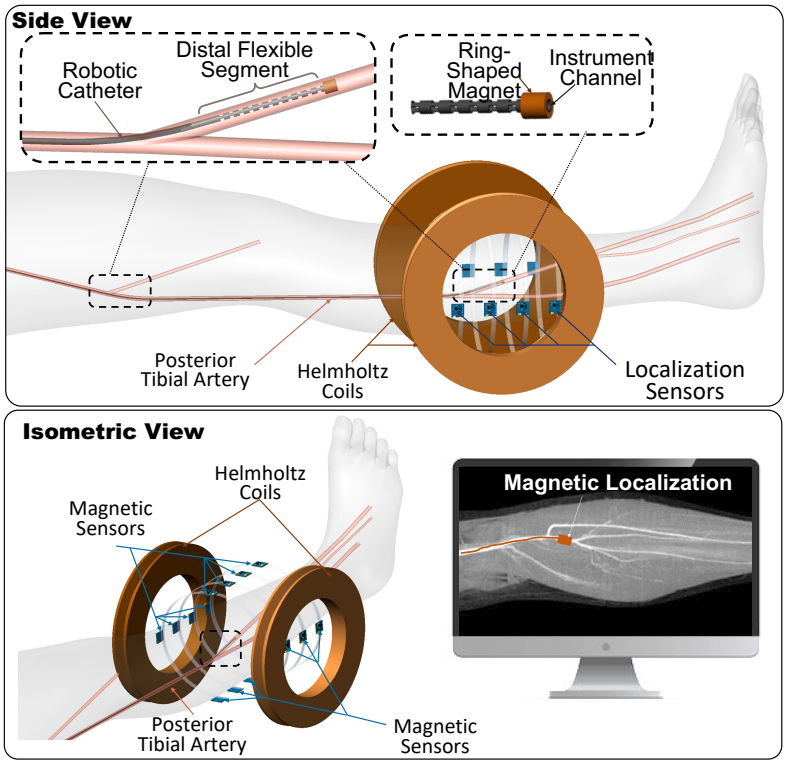

Figure 3.1: Concept illustration of a magnetically steerable robotic catheter MSRC with magnetic localization for peripheral arterial disease (PAD) treatment to reduce X-ray radiation.

distal end of a flexible segment integrated into the catheter. The sensor array was placed within the posterior compartment of the leg.

This model offered a visual representation of the MSRC navigating through complex artery bifurcations and curved pathways. It uses Helmholtz coils to induce a current that guides the catheter along the **XY** plane. Meanwhile, a set of sensors records the magnet's real-time position and generates a dynamic map of its location, making it available to users on their display screens.

3.2 Mathematical Model

This section presents the mathematical modeling for the magnetic localization algorithm. Figure 3.2 depicts a schematic illustrating the parameters involved in the magnet localization algorithm. All vectors marked with the superscript "s" are defined within the sensor-fixed frame, while those without a superscript are referenced in the global coordinate frame.

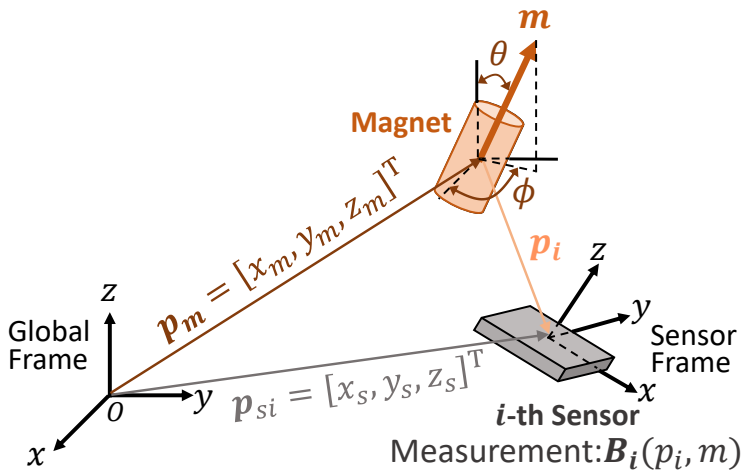

Figure 3.2: A schematic diagram showing the parameters in magnetic localization.

Given that the permanent magnet (PM) within the MSRC is relatively small, and the magnetic sensors are positioned at a considerable distance from the magnet, the magnetic flux density, $\mathbf{B_i} \in \mathbf{R}^3$, at the i-th sensor location can be described as dictated by the dipole model established by Jackson [35].

$$\mathbf{B_i} = \frac{\mu_0}{4\pi}\left(\frac{3(\mathbf{m}^\top \mathbf{p}_i \cdot \mathbf{p}_i)}{\|\mathbf{p}_i\|^5}\right) - \frac{\mathbf{m}}{\|\mathbf{p}_i\|^3}) \ , \tag{3.1}$$

where:

$\mathbf{m}$ = Magnetic dipole moment vector of the PM, $\mathbf{m} \in \mathbf{R}^3$

μ_0 = Magnetic permeability of free space

$\mathbf{p_i}$ = Vector from the center of the magnet to i-th sensor location, $\mathbf{p_i} \in \mathbf{R}^3$

The vector $\mathbf{p}_i \in \mathbf{R}^3$ can be calculated via

$$\mathbf{p}_i = \mathbf{p_{s}}_i - \mathbf{p_m}, \tag{3.2}$$

where $\mathbf{p_{s}}_i = [x_s, y_s, z_s]^\top$ and $\mathbf{p_m} = [x_m, y_m, z_m]^\top$ are the coordinates of i-th sensor and magnet in the global-fixed frame, respectively, as shown in Figure 3.2. The dipole moment vector $\mathbf{m} \in \mathbf{R}^3$ for the PM can be represented as

$$\mathbf{m} = M(\sin\theta\cos\phi\mathbf{i} + \sin\theta\sin\phi\mathbf{j} + \cos\phi\mathbf{k}), \tag{3.3}$$

where $\mathbf{i}$, $\mathbf{j}$, and $\mathbf{k}$ are the unit vectors along the x, y, and z-axes, respectively; θ and ϕ are the angles of magnet's orientation in a spherical coordinate with its origin at the center of the magnet location. θ is the angle of rotation from the z-axis, and ϕ is the angle of tilt from the x-axis, as shown in Fig. 3.2. The dipole moment strength, M of the permanent magnet can be computed using

$$M = \frac{B_r V_m}{\mu_0}, \tag{3.4}$$

where B_r corresponds to the magnetic remanence of the permanent magnet material, and V_m represents the volume of the magnet.

The sensor's location provides measurements of the magnetic flux density along the three axes within its sensor-fixed array. The measured flux density from the sensor array, denoted as ${}^{\mathbf{s}}\mathbf{B_i}$, can be determined through the following equation:

$${}^{\mathbf{s}}\mathbf{B_i} = \mathbf{T_i}\mathbf{B_i}. \tag{3.5}$$

Here, $\mathbf{T_i} \in \mathbf{R}^{3\times3}$ represents the rotation matrix that relates the global coordinate system to the i-th sensor-fixed coordinate system. This matrix is computed based on the sensor's orientation.

3.3 Magnetic Localization Algorithm

The foundation of the magnetic localization algorithm in the MSRC is derived from the work of Taylor et al. [36], and has been adapted to suit the specific requirements of the MSRC application.

Building upon the dipole model discussed in the previous section, a nonlinear optimization problem is formulated to estimate both the position and orientation of the magnet:

$$\hat{\xi} = \arg\min_{\xi} \sum_{i=1}^{N_s} \|^{\mathbf{s}}\mathbf{B_i}(\xi, \mathbf{p_{si}}, M) - {}^{\mathbf{s}}\mathbf{B_i'}\|^2, \tag{3.6}$$

where:

$\hat{\xi}$ = Vector containing estimated magnet position and orientation angles — $[\hat{\mathbf{p_m}}^\top, \hat{\theta}, \hat{\phi}]^\top \in \mathbf{R}^5$

N_s = Number of sensor measurements

${}^{\mathbf{s}}\mathbf{B_i'}$ = Magnetic flux density from the i-th sensor within its local frame

The objective of Equation (3.6) is to minimize the sum-of-squared errors between the predicted magnetic field, as governed by Equation (3.1), and the real measurements.

To address this non-linear optimization problem, the Levenberg-Marquardt (LM) algorithm was selected to optimize (3.6). The LM algorithm is suitable for real-time application given its efficiency in solving nonlinear least-square problems [37].

To achieve low latency while maintaining estimation accuracy, an analytical expression for the Jacobian matrix ($\mathbf{J_i}$) was derived.

$$\mathbf{J_i} = \mathbf{T}_i \frac{\partial \mathbf{B_i}}{\partial \xi}. \tag{3.7}$$

This analytical approach involves taking derivatives of the magnetic field prediction in the sensor frame (3.5).

3.4 Ambient Field Removal

The magnetic field originating from the primary source magnet, as detected from the sensors' local frames, typically records at levels below 8 Gauss, a magnitude similar to Earth's inherent magnetic field. The magnetic field from the primary magnet was about as strong as Earth's magnetic field, therefore further action was taken to reduce any interference or mixing of these magnetic fields.

To address the interference caused by the surrounding magnetic field, a two-step approach was used. First, to record the magnetic field readings when there was no other magnetic source nearby, focusing on capturing only Earth's magnetic field. This data acts as a calibration to understand the surrounding magnetic field. Then, during actual measurements, subtract this recorded background magnetic field from the sensor readings at all measurement points. This subtraction isolates and identifies the magnetic field produced by the primary source magnet.

The measurement of Earth's magnetic field was regularly updated, which serves as a reference for removing the background field. This was necessary in case the Magnetic Source Localization system moves or rotates, as changes in system orientation can cause variations in the background magnetic field. Regular updates

ensured accurate and reliable results.

3.5 Sensor Position and Magnetic Moment Calibration

In the magnetic localization method described in Equation (3.6), it is assumed that the positions of all magnetic sensors ($\mathbf{p_{si}}$) and the strength (M) of the magnet to be localized are known beforehand. However, the actual sensor positions may deviate from their expected locations due to inaccuracies in the mechanical design and assembly process. Additionally, the magnet's true strength may differ from its expected value. To address these disparities, calibration data was collected for an approximated position of the magnet's position and orientation.

One calibration method, as introduced in [13] and the equation below, uses a sequential approach to estimate the magnet's dipole moment (M) and the sensor locations ($\mathbf{p_{si}}$).

$$\hat{M} = \arg\min_{M} \sum_{j=1}^{N_d} \sum_{i=1}^{N_s} \| M \ {}^{s}\bar{\mathbf{B}}_{\mathbf{ij}} - {}^{\mathbf{s}}\mathbf{B}_{\mathbf{ij}}^{'} \|^2, \tag{3.8}$$

$$\hat{\mathbf{p_{si}}} = \arg\min_{\mathbf{p_{si}}} \sum_{j=1}^{N_d} \| {}^{s}\mathbf{B}_{\mathbf{ij}}(\mathbf{p_{si}}, M, \mathbf{p_{mj}}, \theta_j, \phi_j) - {}^{\mathbf{s}}\mathbf{B}_{\mathbf{ij}}^{'} \|^2. \tag{3.9}$$

The optimization in Equation (3.8) minimizes the error between the measured sensor data and the predicted data from the estimated dipole moment and sensor positions.

This process uses assumed sensor positions and iteratively refines them using the estimated dipole moment. The assumed sensor positions were extracted from the system's CAD model. However, this sequential calibration approach may not yield the optimal results due to the interdependence between the two optimization problems.

Equation (3.10) represents this simultaneous optimization problem, to minimize the error between the measured sensor data and the data predicted based on both the sensor positions and the dipole moment. However, this optimization problem is highly nonlinear and computationally expensive.

$$\min_{M,\mathbf{p_{si}},\forall i} \quad E = \sum_{j=1}^{N_d} \sum_{i=1}^{N_s} \| M \ {}^{s}\bar{\mathbf{B}}_{\mathbf{ij}}(\mathbf{p_{si}}) - {}^{\mathbf{s}}\mathbf{B}'_{\mathbf{ij}} \|^2. \tag{3.10}$$

To overcome the computational challenges and maintain accuracy, a new calibration method was proposed. This method implements a nested framework, as depicted in Fig. 3.3, to estimate the magnetic dipole strength (M) and sensor positions ($\mathbf{p_{si}}$). For each possible value of the magnetic dipole moment (M_k) within a

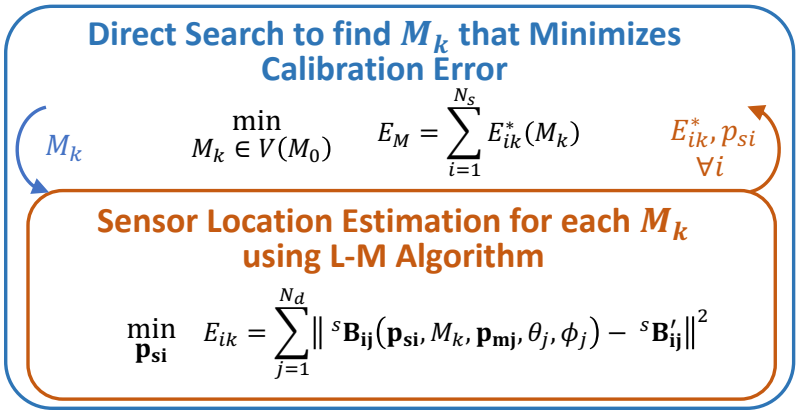

Figure 3.3: The proposed new nested calibration method for magnetic dipole strength and sensor positions.

feasible range, the sensor location estimation problem is solved. The optimal dipole moment ($\hat{M}$) is then determined using a direct search approach that minimizes the localization error across all sensors. Subsequently, the optimal sensor positions ($\hat{\mathbf{p_{si}}}$) are found based on the results of the sensor location estimation with $\hat{M}$.

This nested calibration approach effectively addresses the interdependence

between the two optimization problems, maintains computational efficiency, and ensures optimality. Compared to the sequential and simultaneous estimation methods, this proposed approach offers improved performance, as demonstrated in Section 5.2.

3.6 Actuation Implementation

To develop the actuation algorithm, the MSRC underwent testing with varying current levels to determine the tilt angle. A grid and protractor-marked plate replaced the base of the sensor array track, and the catheter distal's base was secured to the center of the global frame, as depicted in Figure 3.4.

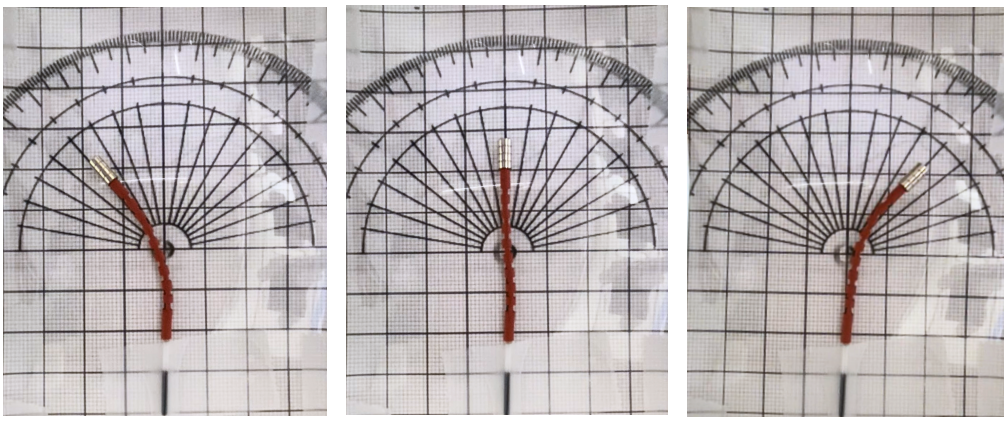

Figure 3.4: Catheter on protractor marked plate to measure tilt angle with varying duty cycles. a) Maximum tilt in $-\mathbf{x}$ direction, b) Initial position, c) Maximum tilt in $+\mathbf{x}$ direction

The duty cycle in the power source was incrementally increased by 0.1, and the resulting angle of the magnet on the $\mathbf{y}$-axis was recorded. This procedure was repeated three times for both $+\mathbf{x}$ and $-\mathbf{x}$ directions. The results are illustrated in

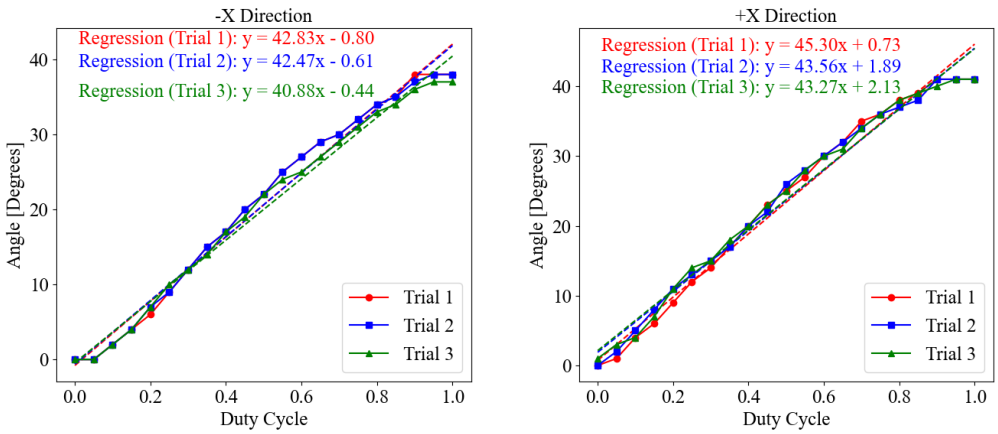

Figure 3.5: Data testing MSRC steering angle at various duty cycles to both directions and their calculated linear regressions. a) Testing for $-\mathbf{x}$ direction steering b) Testing for $+\mathbf{x}$ direction steering

Figure 3.5.

The graph reveals a consistent linear relationship between the angle and duty cycle. The calculated slope and intercept from these linear regressions were summarized in Table 3.1. Peripheral arteries are expected to exhibit a bifurcation angle of 30°, therefore the maximum turning angle of 43° fits the maneuverability parameters. The average of the linear regressions from the trials yields the following relationship:

$$\boldsymbol{\alpha} = 43.044\ \mathbf{D} + 0.481, \tag{3.11}$$

where $\boldsymbol{\alpha}$ is the angle from the $\mathbf{y}$-axis and $\mathbf{D}$ is the duty cycle. This tilt angle, α, results in displacements in both the $\mathbf{x}$ and $\mathbf{y}$ directions, forming a right-angle triangle, as shown in Figure 3.6.

Table 3.1: Average Linear Regression for Magnetic Steering from Duty Cycle.

Direction	Trial #	Slope	Intercept
$-\mathbf{x}$	Trial 1	40.833	-0.442
$-\mathbf{x}$	Trial 2	42.831	-0.797
$-\mathbf{x}$	Trial 3	42.468	-0.615
$+\mathbf{x}$	Trial 1	43.558	1.887
$+\mathbf{x}$	Trial 2	45.299	0.732
$+\mathbf{x}$	Trial 3	43.273	2.126
	Average	43.044	0.481

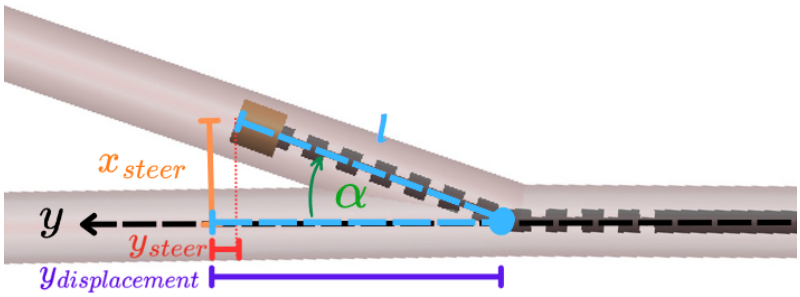

Figure 3.6: Diagram for catheter geometry during steering for actuation calculations

The derived equations for $\mathbf{y_{steer}}$, $\mathbf{x_{steer}}$, and $\mathbf{\Delta y}$ are:

$$\mathbf{y_{steer}} = l(l - \cos\alpha), \tag{3.12}$$

$$\mathbf{x_{steer}} = l\sin\alpha, \tag{3.13}$$

$$\mathbf{\Delta y} = y_{displacement} - y_{steer}, \tag{3.14}$$

where $y_{displacement}$ is the total displacement of the catheter given by the feeding mechanism, assuming the zero position is with the magnet at the center of the bifurcation partition. Additionally, y_{steer} is the displacement in the $\mathbf{y}$ axis due to the turning angle of the magnet, l is the length of the catheter distal with the magnet tip that turns, and α is the tilt angle from the induced current. These relationships were implemented into the LabView code to introduce actuation tracking into the navigation. Figure 3.7 shows the logic for implementation of equations (3.13), (3.12), and (3.14).

Figure 3.7 depicts the encoder readings from the catheter feeding mechanism sent as an analog input to the Tracking and Sensing myRio. The feeding was led by the dial of the catheter feeding mechanism connected to the translation encoder, and the steering was led by the dial with the steering encoder. The translation encoder readings were transformed into displacement readings by taking into account the encoder and motor specifications, such as encoder resolution, pulse angle, and number of phases. Then the displacement per step was calculated, and an additional gain was added for fine-tuning, equating to the total feed displacement. Once the steering is activated, the y_{steer} was subtracted from $y_{dispalcement}$ to get the change in y movement and plot the new y-coordinate. The steering encoder analog read is transformed to the duty ratio, which is sent to the Helmholtz coils. The tilt angle, α, is calculated from the duty ratio by using Eq. (3.11). This angle is used to calculate

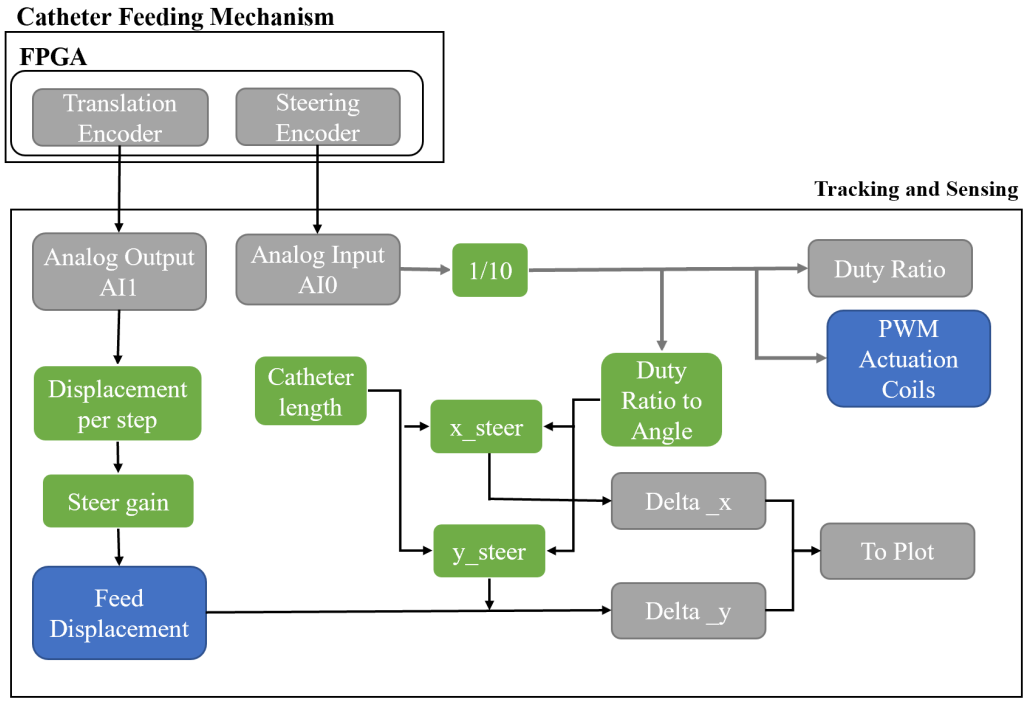

Figure 3.7: Conceptual diagram for implementation of derived equations, $\mathbf{x_{steer}}$ and $\mathbf{y_{steer}}$, using LabView

the x_{steer} and y_{steer} using equations (3.13) and (3.12) respectively. Then the change in position is recorded and plotted.

The algorithm required testing the MSRC at varying current levels to determine the tilt angle. A linear relationship was established between the angle and duty cycle, with a calculated relationship represented by Eq. (3.11). This tilt resulted in displacements in both the $\mathbf{x}$ and $\mathbf{y}$ directions, as described in Equation (3.12). These findings enabled the integration of actuation tracking into the MSRC's navigation system, enhancing its maneuverability and control during medical procedures.

Chapter 4

Experimental Set-Up

Figure 4.1 provides an illustration of the MSRC prototype system that combines magnetic steering and localization. Left: hardware prototype comprising a catheter with a flexible distal segment and ring-shaped magnet adhered at its tip, Helmholtz coils for magnetic steering, a catheter feeding mechanism, a control box, a frame with 16 magneto-resistive sensors for catheter tip localization, a real-time controller for the system. Right: three 3D-printed phantoms for leg vasculature and catheter tip. This system consists of several components:

1. Magnetic tip
2. Flexible catheter distal
3. Catheter feeding mechanism.
4. Magnetic sensor array.
5. Helmholtz coils as steering mechanism.
6. Three distinct vasculature models.

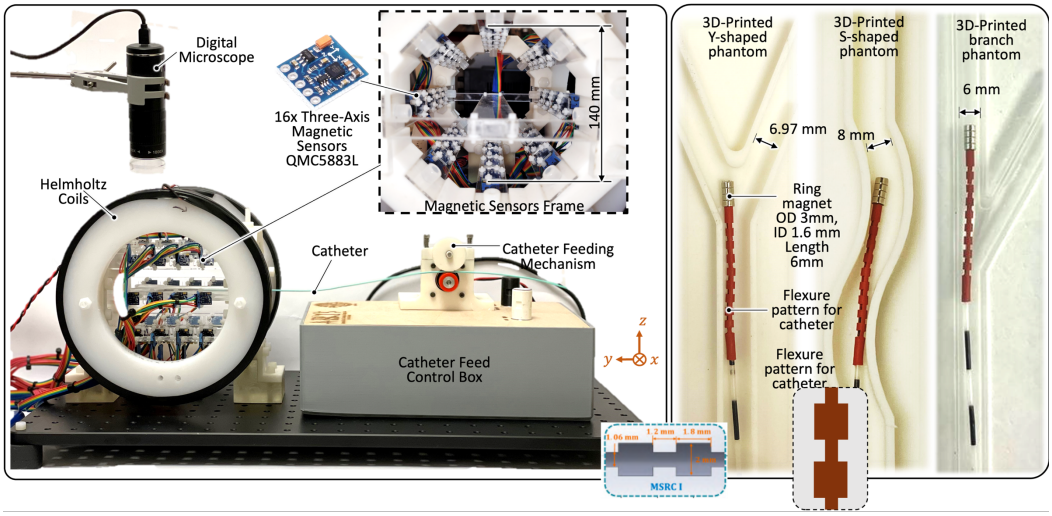

Figure 4.1: Photograph of the magnetically steerable robotic catheter prototype and subsystems.

4.1 Magnets

Permanent magnets are graded based on their maximum energy output, with higher magnet grades indicating greater magnetic strength. The grade of a permanent magnet signifies its ability to generate and retain magnetic force. Pull strength, on the other hand, represents the actual force that the magnet can exert when in direct contact with a ferrous material. Three different sized and geometrically different agents were analyzed for accuracy and saturation within the sensor array as seen in Table 4.1.

Table 4.1: Alternative Permanent Magnets

Number	Shape	Dimension	Grade	Pull Force [lbf]
1	Cylindrical	3/16" OD, 3/8" L	N42	0.44
2	Cylindrical	1/8" OD, 1/4" L	N52	1.66
3	Cube	1/4" L	N52	5.26

Two cylindrical and a cube magnet were tested in the cylindrical array. The readings were analyzed to visualize if the pull force caused saturation or if it was

sufficient to be detected by the sensors. Magnet 3's geometry is too big for the vasculatures, but it served as a model to visualize high pull force, which resulted in saturation of the sensors. Magnet 1 did not have enough pull force to be accurately read by the sensors, causing too much noise in the readings. Magnet 2 had the correct dimensions for vasculature navigation and enough pull force for the sensors to read accurately. Four Magnet 2 units were stacked together and placed at the end of the catheter distal. Each of the magnets was N52 NdFeB of 3.175 mm outer diameter, 1.6 mm inner diameter, and 2 mm tall. Magnet 2 has a high residual flux density of 14800 Gauss. The Grade N52 magnets are coercive, but they experience reduction in magnetic performance at elevated temperatures over 80°C. The ring shape allows for a device within the instrument channel to travel, such as passing a balloon for PAD procedure.

4.2 Catheter

The catheter design was limited to the geometry of the posterior arteries and bifurcations. Bifurcations are 5-6.5 mm in diameter, the femoral artery is 5-8mm, and the popliteal artery is 5-6.5mm in diameter [38]. Given these anatomical constraints, an effective magnetically-controlled robotic catheter must meet the following criteria:

1. Ability to navigate within arteries less than 6 mm in diameter,
2. Ability to maneuver through artery bifurcations of 30°,
3. Open instrument channel for accommodating instruments like stents,
4. Integration of a compact electromagnetic actuation for controlling catheter bending and insertion without altering surgical procedures.

The design for a flexible catheter was inspired by kirigami art by implementing slits on each side of the distal [2]. Heat shrink tubing was used as the material of choice due to its structural strength and flexibility. The process involved selecting appropriately scaled heat shrink tubing, designing and optimizing the flexure patterns, and adhering the tubing to a commercial catheter after cutting.

4.3 Feeding Mechanism

The feeding mechanism in Figure 4.2 uses a friction drive system [2], consisting mainly of an idler wheel responsible for positioning and pressing the catheter, and a drive wheel to push the catheter's feed movement through friction. The drive wheel was created with a layer of Urethane sleeves on its outer surface, enhancing its effectiveness in propelling the catheter. The idler wheel contains a V-shaped groove to guide the catheter laterally. To reduce wear on the catheter and drive wheels, the idler wheel was designed from a low-friction solid polymer, allowing the catheter to glide smoothly without causing damage. The motion of the drive wheel was controlled by a stepper motor. The force applied by the feeding mechanism to translate the catheter was determined by the maximum frictional force between the drive wheel and the catheter.

The feeding mechanism is connected to two encoders, one for feeding and one for steering. The feeding mechanism also has its own myRio, separate from the one of the sensor array. The output of the steering encoder was connected to the sensor's myRio and adjusted to output the desired duty cycle. The signal from the feeding encoder was manipulated using the encoder and motor's specifications to transform the analog reading to a discrete catheter position.

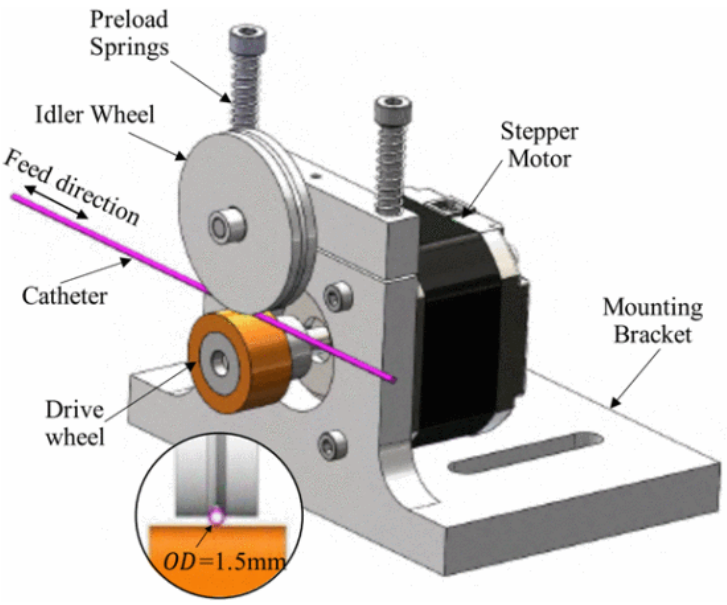

Figure 4.2: Friction drive design for catheter insertion, adapted from [2]

4.4 Sensors

A cylindrical array of magnetic sensors was designed to encircle the catheter's tip, as visualized in Fig.4.1. A high-resolution magnet-resistive sensor, QMC5883L, with a resolution of 5 mGauss and a measurement range extending up to ±8 Gauss, was selected.

Within the prototype system, a total of 32 sensors were symmetrically positioned in the cylindrical array, each spaced 25 mm apart along the **y**-axis. This specific cylindrical sensor array design catered to scenarios involving lower-limb treatment. Only 16 of these sensors were utilized, which encompassed the top,

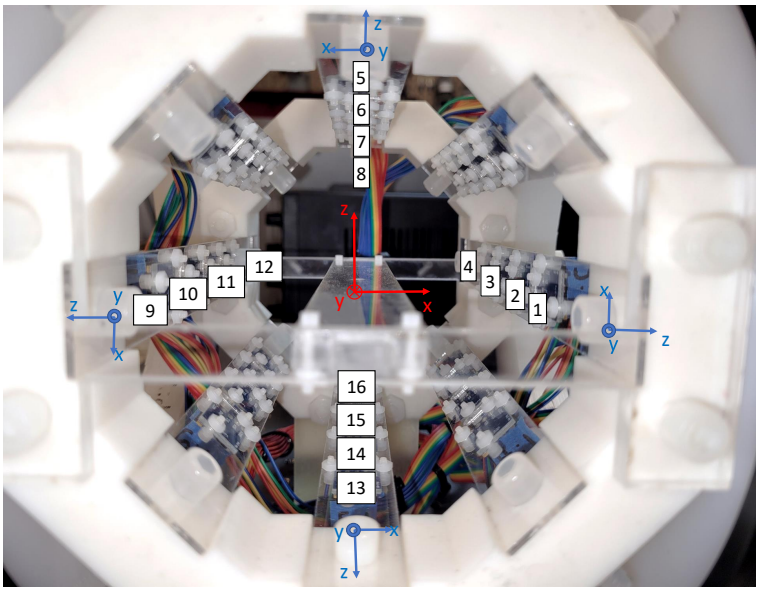

Figure 4.3: Diagram of sensor layout within testing apparatus with the reference frame of each sensor orientation and global frame for magnet testing

bottom, left, and right columns. This sensor layout was chosen to streamline the instrumentation and computational processes, ensuring operational efficiency.

The global frame's origin was situated at the center of the apparatus, with the **y**-axis extending along the bridge and into the apparatus. The base of each sensor was directed toward the central bridge. These sensors each had their own reference frame, which could vary based on their orientation around the bridge. Figure 4.3 provides a visual representation of the global frame located at the center of the apparatus, along with the reference frame for each sensor array. The orientation of the sensor reference frames was subsequently adjusted to align with the global frame. No sensor was directly placed at the axes' origin.

To improve data fidelity, an oversampling technique was applied to all sensor signals, reducing the impact of noise. These sensor signals were collected by a National Instruments myRIO real-time controller and routed through the I^2C interface.

The data collection process introduced a minimal latency of only 5 ms.

The real-time magnetic localization and actuation algorithms, which are discussed in more detail in Section 3.3, were implemented within the myRIO real-time controller, as seen in Appendix A. This configuration ensured a computation latency of approximately 400 ms, which proved more than adequate for delivering timely feedback and facilitating real-time decision-making for the human operator.

4.5 Helmholtz coils

The magnetic actuation of the catheter utilizes Helmholtz coils. the distance between the coils was equal to their radius to generate a uniform linear magnetic field between the coils [38]. This actuation mechanism combats the need for a large magnetic field from the large distance between the magnetic source and the permanent magnet.

The magnetic flux of the coils can be represented as [39]

$$B = \frac{8}{5\sqrt{5}} \frac{\mu_0 N I}{R_c}, \tag{4.1}$$

where

$\mu_0 = 4\pi \times 10^{-7} \mathrm{T} \cdot \mathrm{m/A}$ as the permeability of free space

$N =$ Number of turns in the coil

$I =$ Current amplitude in coils

$R_c =$ Coil radius

The small-sized magnet is modeled as a magnetic dipole with a moment from Equation (3.4). When current is applied to the coils, they produce a steering torque applied to the PM. This current controls the direction of the catheter's distal

segment. The steering torque is calculated as [38]

$$T_m = MB\sin\theta, \tag{4.2}$$

where

θ = Angle between magnetic dipole moment and external magnetic field

M = PM Dipole Moment

B = Coil magnetic flux density

The Helmholtz coils constructed have a diameter of 220 mm, with 120 turns each. They are placed on each side of the sensor array, 110 mm apart, and are connected in series with a maximum allowed current amplitude of 11 A. They are driven by a full-bridge, bi-directional, power amplifier.

4.6 Vasculature Models

Three vascular models were fabricated to evaluate the maneuverability of the MSRC as depicted in Figure 4.4. All of these phantoms were positioned at the center of the sensor array.

A Y-shaped bifurcation in Figure 4.4.a incorporates a narrow 7 mm opening. The bifurcation angles were set at 20° from the **y**-axis. This particular bifurcation served as a means to evaluate the real-time accuracy of the MSRC's movements once integrated with LabView tracking.

The S-shaped phantom in Figure 4.4.b uses a wider 8 mm opening, printed on white SLA. This phantom was designed to assess the catheter's ability to navigate along curved paths in the **XY** plane during actuation, by aligning the magnet perpendicular to the phantom's border.

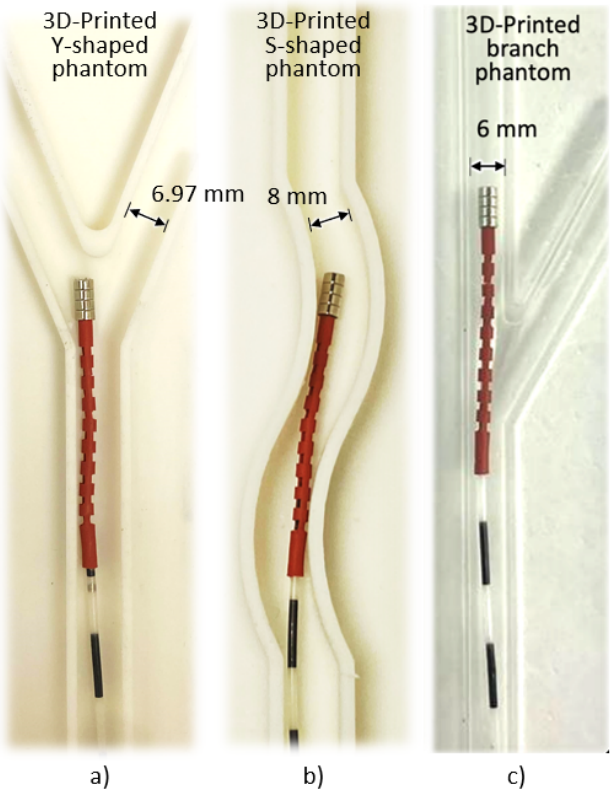

Figure 4.4: Pictures of the printed vasculature models for navigation testing. a) Y-shaped phantom. b) S-shaped phantom. c)Branch Phantom

Lastly, the Branch phantom in Figure 4.4.c features a smaller 6 mm channel. This model comprised a straight channel along the **y**-axis with a 30° branch. It was utilized to assess the tracking and actuation capabilities when implemented in real-time within LabView. The accuracy of sensing and actuation was tested under this narrower and higher turn vasculature.

4.7 Layout

The integration of the hardware, as depicted in Figure 4.1, presented a comprehensive visual of its assembly. The Helmholtz coils were positioned on either side of the sensor array's **x**-axis. The catheter entered the sensor array through the designated opening, following the **y**-axis, while the Helmholtz coils facilitated turning along the **x**-axis within the **XY** plane. Notably, the catheter featured a flexible distal end, equipped with a configuration of ring-shaped stacked magnets.

The catheter's feeding and turning movements were controlled by the catheter feeding mechanism. This mechanism comprised both feeding and turning dials, each with the capacity to regulate the extent of catheter deflection and the amount of current supplied by the coils.

Chapter 5

Experimental Evaluation

5.1 Magnetic Localization and Calibration Experiments

The localization and calibration process utilized two SLA-printed calibration grids. These grids were manufactured with a machining accuracy of 0.025 mm. The plate layouts were configured to position magnets both in straight and angled orientations relative to the **y**-axis of the global frame. The angled plate had a 30° inclination from the **y**-axis. Each magnet was situated 10 mm apart from its neighboring magnets along both the **XY**-axes. For the initial calibration, the plates were structured as a 3×17 grid. as seen in Figures 5.1a and 5.2a.

For localization, the magnetic sensor readings were obtained at all 51 locations on the Calibration Plate 1, as illustrated in Fig. 5.1a. Data in Fig. 5.1 was used for calibration of the true sensor locations. The sensor array encompassed magnet positions ranging from -40 to 40 mm on Calibration Plates 1 and 2. Figure 5.1b displays the magnetic localization results assuming the nominal sensor positions. Notably, the estimation error for magnet position was smaller within the central section of the plate when situated under the sensor array, with x in the range of

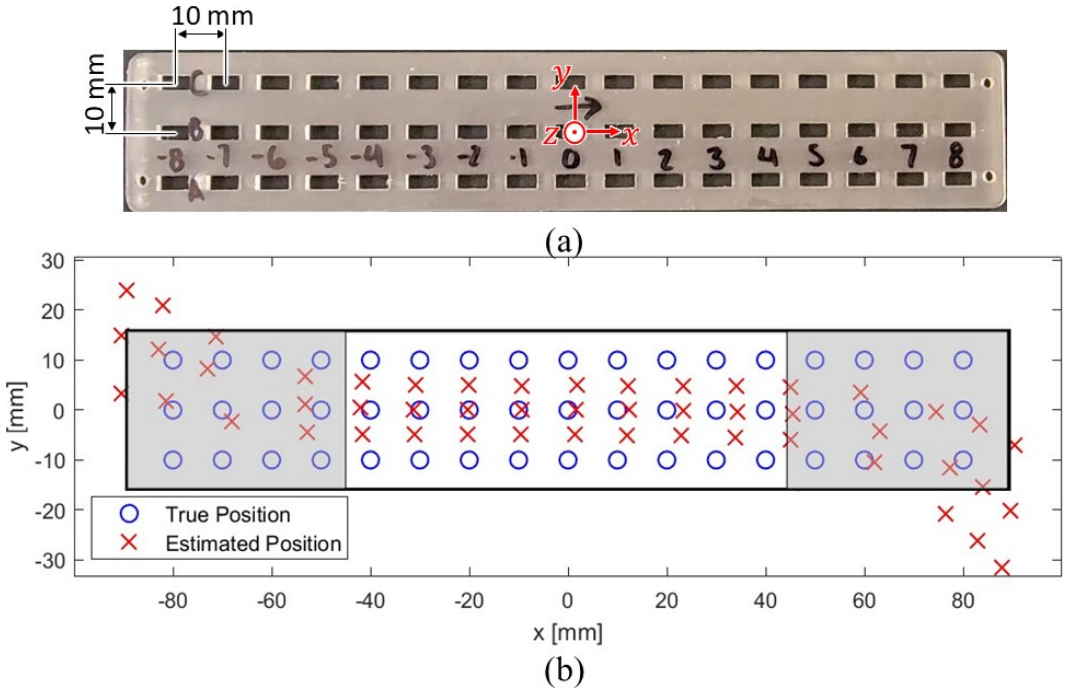

Figure 5.1: Magnetic localization before sensor location calibration. (a) Photograph for the 3D-printed Calibration Plate 1. (b) Comparison between the true and estimated magnet locations using Calibration Plate 1 before sensor location calibration

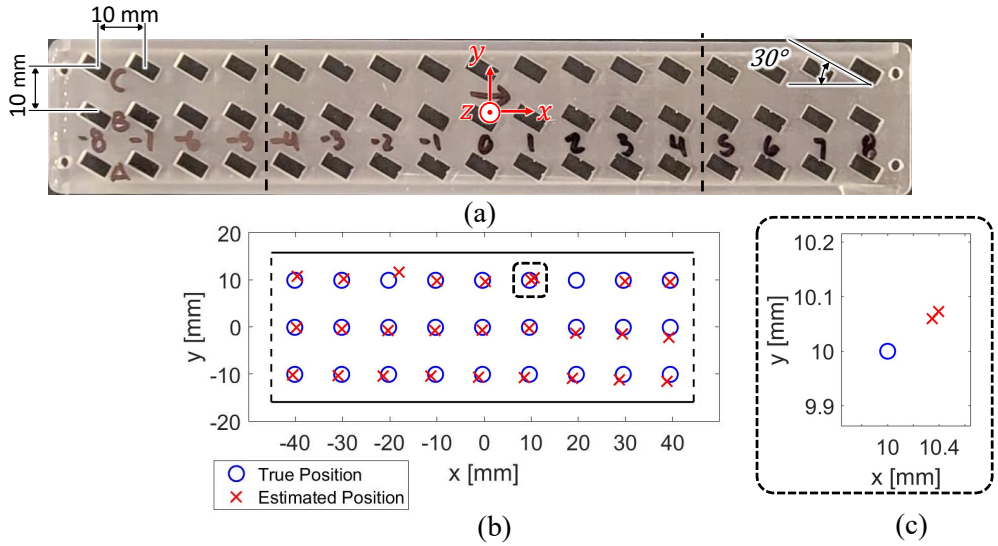

Figure 5.2: Magnet location estimation data on Calibration Plate 2 after sensor location calibration. (a) Photograph of Calibration Plate 2. (b) Calibrated estimated magnet positions. (c) Zoom-in view of outlier data.

Table 5.1: Average Localization Error

Data Range	w/o calib.	w/ [13] calib.	w/ nested calib.
All (51 pts) xyz	10.16 mm	5.28 mm	4.53 mm
All (51 pts) ϕ	6.07°	3.20°	3.77°
All (51 pts) ϕ	12.48°	8.52°	8.62°
Center (27 pts) xyz	4.34 mm	1.74 mm	0.95 mm
Center (27 pts) θ	1.46°	0.98°	1.00°
Center (27 pts) ϕ	3.84°	3.08°	1.75°

$x \in [-40 \text{ mm}, 40 \text{ mm}]$. Beyond the sensor array, the error increased to 20 mm at the plate's edge due to a reduction in the signal-to-noise ratio in the sensor readings. Therefore, to acquire high-quality signals for precise magnet localization, it was imperative for the sensor array to cover the magnet locations. The localization error in the **y**-axis was also observed to be biaseds towards the same direction as the magnet location, particularly at the two ends of the Calibration Plate 1. This bias is attributed to a combination of errors in the magnet's magnetization axis and the parallelism between the sensor frame and the Calibration Plate 1.

To validate the performance of sensor location calibration, the magnet was placed on Calibration Plate 2 at angled positions, as shown in Fig. 5.2a. Figure 5.2b presented the magnetic localization results after calibration, with an outlier noted in the box location (20,10) mm in Figure 5.2c. The results of localization before and after calibration on the straight and angled plates (Calibration Plates 1 and 2) are provided in Table 5.1.

Table 5.1 presented the average localization errors without calibration, with calibration, and with the nested calibration for the entire range of the test plate and the center range. When comparing magnet position localization on the entire Calibration Plate 2 before and after calibration, the mean error decreased from 10.16 mm to 4.53 mm. As previously discussed, localization over the entire plane

includes the outliers of the plate's extremities that are out of the cylindrical sensor array. Within the sensor array, specifically in the central columns, a substantial improvement in accuracy was evident, with the mean error in position localization decreasing from 4.34 mm to 1.74 mm after calibration, and further to 0.95 mm with nested calibration. This demonstrated that the algorithm successfully localized a magnet's position within an average distance of 0.95 mm within the sensor array's coverage. In the center range, the θ error experienced a slight increase of 0.02°, while the ϕ, representing the magnet's orientation, improved from an error of 3.08° to 1.75°.

5.2 MSRC Navigation Sensing Experiments

The conducted experiment involved catheter insertion into the bifurcations, allowing it to enter through one of the channels, retracting, activating the coils to bend the magnet in the opposite direction, further inserting the magnet, and resuming sensing. Figure 5.3 depicted the steps taken during the physical recording and data acquisition for MSRC navigation.

Figures 5.3 and 5.4 are snapshots of the prototype navigating different vasculature models using localization without the tracking during actuation. The process, as depicted in Figure 5.3, illustrated the magnet's movements. In frame (a), the magnet entered the branch at zero seconds, marking the initial location on the localization. The magnet then moved along the bifurcation in (b), entered the top branch without additional steering or actuation in (c), and reached its maximum localization in (d). The path taken by the magnet was continuously recorded in real-time by the localization and compared at each frame. Once the magnet reached the top position, it was retracted back to its starting location (e). The localization indi-

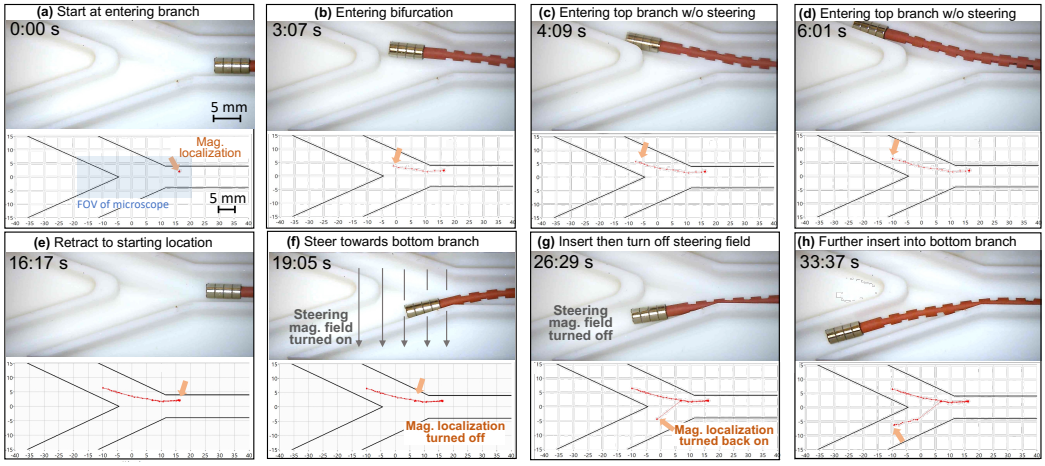

Figure 5.3: Snapshots of digital microscope video for the prototype magnetically steerable robotic catheter navigating through the 3D-printed vascular phantom with 20° bifurcation and the screenshots of the user interface showing the catheter tip location estimation using magnetic localization.

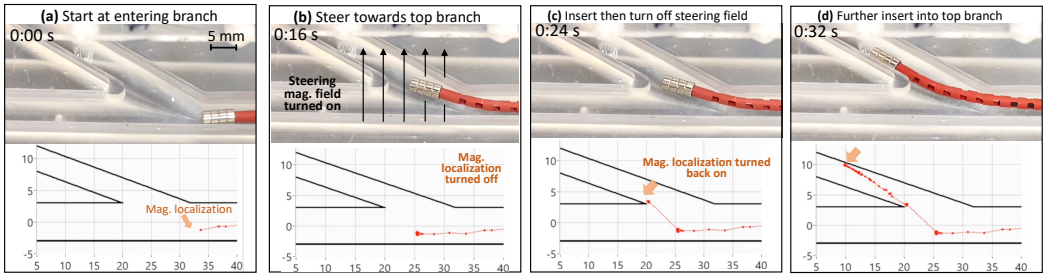

Figure 5.4: Snapshots of the prototype magnetically steerable robotic catheter navigating through the 3D-printed vascular phantom with a 30° bifurcation.

cated that the magnet followed the same path during retraction and returned to the initial location. Subsequently, the magnet was maneuvered forward onto the bifurcation, and the steering magnetic field was activated to bend the flexible catheter in the direction of the lower branch (f) as it was inserted. While the steering magnetic field was active, the localization function was turned off. After the magnet entered the bottom branch, the magnetic field was deactivated, and localization was reactivated, detecting the new position of the magnet and establishing a linear estimation of its path (g). The magnet was then further inserted into the bottom branch, with its final position recorded in the localization.

The process was first tested on the Y-shaped bifurcation, Figure 5.3, with an angle of separation of 20° and a channel diameter of 7 mm, then verified with a straight channel with a 30° branch-off and a smaller channel diameter of 6 mm, as seen in Figure 5.4. Using the branch-off phantom, the magnet started at a retracted position. Before the bifurcation, it moved straight forward in sensing, as depicted in frame (a). Once it reached the separation point, the sensing was turned off and actuation was turned on (b). As the catheter was secured in the branch, actuation was turned off (c), and sensing was resumed (d). The steering dial and feeding dials were used simultaneously to slowly move the magnet onto the upper branch.

The sensing navigation experiment proved the effectiveness of integration in magnetic steering and localization sensing. This method lacks in tracking the magnet's position when the sensors are turned off. During the actuation, the magnet translates 10 mm on the x-axis and 5 mm on the y-axis that are not tracked.

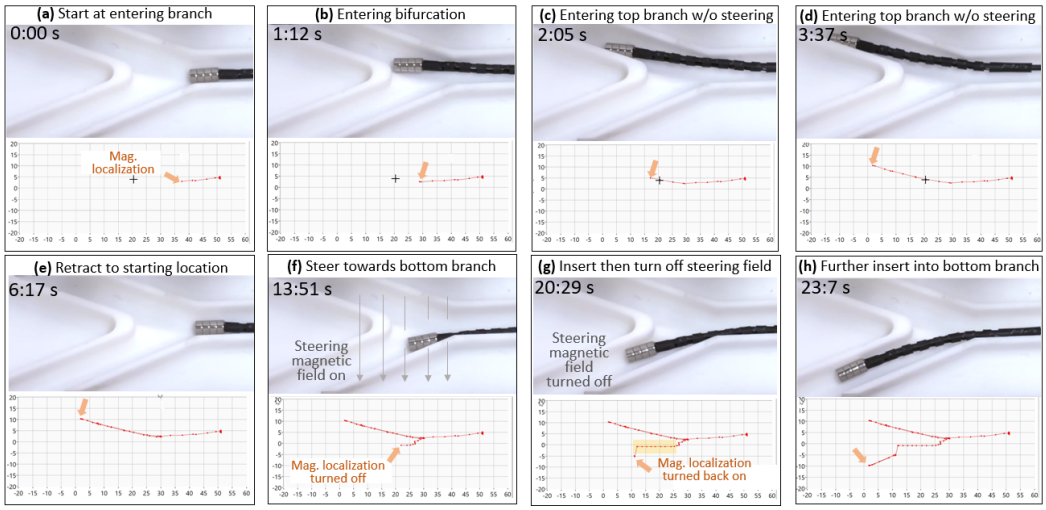

Figure 5.5: Snapshots of digital microscope video for the prototype magnetically steerable robotic catheter navigating through the 3D-printed vascular phantom with 20° bifurcation and the screenshots of the user interface showing the catheter tip location estimation using magnetic localization and tracked actuation.

5.3 MSRC Navigation Integrated Sensing and Actuation Experiments

The catheter motor driver introduced in Section 4.3 was used to control the movement of the catheter. To ensure the correct initialization of actuation and alignment with the sensing, the actuation feeding and steering encoders are reset, and the catheter was manually moved forward to the global zero position.

To improve accuracy on the **y**-axis, the Calibration Plates 1 and 2 were increased from 3 to 5 columns, creating a total of 85 magnet positions that were used for sensor localization and calibration as previously introduced in Section 5.1.

To integrate the sensing and actuation within the LabView navigation code, Eq. (3.11) and Eq. (3.12) were implemented into the tracking algorithm and can be seen in Appendix A. The navigation process, as depicted in Figure 5.5, was

similar to the previous from Figure 5.3. The process differs starting in frame (f) where actuation is activated and tracked as seen in the snapshot of the user interface. Once the catheter was secured in the lower branch as seen in frame (g), the magnetic field was deactivated, and localization was reactivated, detecting the new position of the magnet (g). The highlighted portion in frame (g) uses the actuation model from Section 3.6 to compute the catheter's position. During this process, the tracker approximates the location of the magnet using the Equations (3.13), (3.12), and (3.14). Once the magnet was inserted into the branch, actuation was turned off, and sensing was turned on. The MSRC was further inserted into the branch, and then retracted to the separation point.

This test validates the effectiveness of the proposed method integrating magnetic steering and magnetic location sensing for MSRCs to minimize x-ray radiation for catheter navigation.

Chapter 6

Conclusion and Future Work

The navigation simulations have demonstrated the feasibility of using the MSRC in surgical procedures aimed at treating peripheral arterial disease. Building on this foundation, future work will focus on enhancing the calibration of sensor localization to achieve higher precision, enabling three-dimensional actuation and sensing to extend the capabilities of the MSRC across the **XYZ** axes. This technology will advance the application of MSRC technology in minimally invasive surgical interventions, offering benefits in terms of precision and efficiency. The upcoming sections will delve into these future research directions in detail, elaborating on the potential implications and advancements they may bring to the field of medical robotics and intervascular procedures.

6.1 Contributions

The contribution of the author in this work includes:

- Developed MATLAB code for sensor orientation to the global frame and analyzed data from exported files.

- Data processing from the sensor array.
- Processed data from the sensor array to assess position accuracy for various magnet sizes and shapes.
- Development of MATLAB code for ambient field removal.
- Adaptation of Jacobian, backwards, and forwards position estimation codes for sensor calibration.
- Designed and fabricated vasculature phantoms for testing.
- Design of hardware to stabilize catheter feeding.
- Determined catheter feed rates based on the encoder and motor specifications.
- Developed algorithm to calculate catheter displacement due to steering and feeding.
- Conducted tests to evaluate the repeatability of the catheter's turning angle based on the duty cycle.
- Tested the accuracy of navigation using experimental and user interface views.
- Integrated displacement algorithm from actuation and localization in LabView.
- Enhanced the LabView user interface for improved usability and transition between sensing and actuation.
- Successfully integrated two myRIO devices into a single cohesive project.

6.2 Future Work

6.2.1 Weighted Calibration Algorithm

While the current algorithm effectively considers the translational positions of the sensors and the magnetic strength of the magnet, introducing sensor orientation into the calibration process would likely lead to more accurate results.

Accounting for the orientation of the sensors would provide a more comprehensive calibration approach, further improving the overall performance of the magnetic localization system.

Moreover, future developments should focus on addressing the coupled optimization of multiple parameters, including sensor location, orientation, and magnet properties. This holistic approach would enable a more sophisticated and refined calibration process. The calibration algorithm would then yield more precise and robust results, enhancing the reliability of the magnetic localization system.

Additionally, in future calibration efforts, the incorporation of weights for the center-range magnet positions, especially those in close proximity to their nominal locations, would be advantageous. Assigning different weights to these positions can provide a more accurate calibration, as it acknowledges the varying importance of different magnet positions within the sensor array. This weighted calibration strategy would allow for a more nuanced and targeted optimization, ensuring that critical regions within the sensor array receive the appropriate attention, ultimately improving the system's accuracy and reliability.

6.2.2 Catheter Distal Turning Angle

In the current state of the catheter system, there is a limitation on the maximum achievable turn angle, capped at 40°. To enhance the catheter's maneuverability for navigating complex artery geometries, future work could be directed toward addressing this constraint. One approach could involve further investigation and testing of various flexure patterns, building upon the research conducted in a prior study [2]. Exploring and refining different flexure patterns can potentially contribute to achieving a higher angle of turn, thereby extending the catheter's range

of motion.

Another avenue for expanding the turn angle capability of the catheter involves exploring alterations to the material used in the catheter's distal segment. By considering alternative materials and their mechanical properties, it may be possible to enhance the catheter's flexibility and, consequently, its ability to make more substantial turns. Such an improvement would be particularly valuable for applications where navigating through intricate and tightly curved artery geometries is essential.

6.2.3 Z-axis Movement

The current system operates within the **xy** plane, allowing catheter movement in two dimensions. However, biological vasculatures within the body exhibit three-dimensional motion capabilities in the **XYZ** space.

In the pursuit of achieving three-dimensional catheter motion, the expansion of data points becomes essential. This entails extending the grid plates used in previous experiments to capture data in the **z**-axis, thereby incorporating the full **XYZ** motion range. This extension would enable the system to gather comprehensive data, accounting for movements in all three spatial dimensions, thus, resulting in a more realistic catheter model for the simulation of its navigation through the complex and dynamic vasculatures.

Furthermore, to complement this expansion and achieve effective actuation along the **z**-axis, an additional set of Helmholtz coils will be implemented. These coils will be positioned perpendicular to the existing ones to provide actuation capabilities both upwards and downwards. This development will ensure that the catheter system can navigate not only laterally within the **XY** plane but also incorporate vertical movement along the **z**-axis. The combined efforts of extended data

points and enhanced actuation mechanisms will pave the way for a more comprehensive and realistic simulation of catheter navigation within the human vasculature, promising significant advancements in the field of medical robotics and interventional procedures.

Appendix A

MATLAB and LabView Code

The MATLAB and LabView code can be found on the following repository:
`https://github.com/Ithza-Lopez/Magnetically-Steerable-Robotic-Catheter`

The repository contains the raw MATLAB files used for sensor localization and calibration, as well as testing files to calculate the displacement per step in the encoders of the feeding mechanism. The "SensingAndActuation" folder contains the LabView and code with its MATLAB dependencies. The project makes use of two myRio's runnig simultaneously to connect the feeding mechanism with the sensors and Helmholtz coils.

Bibliography

[1] "Peripheral artery angioplasty." https://my.clevelandclinic.org/health/diseases/17357-peripheral-artery-disease-pad. Accessed: September 20, 2023.

[2] T. G. Mohanraj, J. Song, M. R. Rajebi, L. Zhou, and F. Alambeigi, "A kirigami-based magnetically steerable robotic catheter for treatment of peripheral artery disease," in *2022 9th IEEE RAS/EMBS Int. Conf. for Bio. Robotics and Biomechatronics (BioRob)*, pp. 1–6, IEEE, 2022.

[3] "Centers for disease control and prevision: Peripheral arterial disease (PAD)." https://www.cdc.gov/heartdisease/PAD.htm. Accessed: February 19, 2023.

[4] U. Campia, M. Gerhard-Herman, G. Piazza, and S. Z. Goldhaber, "Peripheral artery disease: past, present, and future," *The American journal of medicine*, vol. 132, no. 10, pp. 1133–1141, 2019.

[5] M. H. Shishehbor and M. R. Jaff, "Percutaneous therapies for peripheral artery disease," *Circulation*, vol. 134, no. 24, pp. 2008–2027, 2016.

[6] "SwiftNINJA Steerable Microcatheter." https://www.merit.com/peripheral-intervention/delivery-systems/microcatheters/swiftninja-steerable-microcatheter. Accessed: September 2021.

[7] M. Khoshnam and R. V. Patel, "Robotics-assisted control of steerable ablation catheters based on the analysis of tendon-sheath transmission mechanisms," *IEEE/ASME Transactions on Mechatronics*, vol. 22, no. 3, pp. 1473–1484, 2017.

[8] L. Wang, D. Zheng, P. Harker, A. B. Patel, C. F. Guo, and X. Zhao, "Evolutionary design of magnetic soft continuum robots," *Proc. Natl. Acad. Sci. U.S.A.*, vol. 118, no. 21, p. e2021922118, 2021.

[9] L. B. Kratchman, T. L. Bruns, J. J. Abbott, and R. J. Webster, "Guiding elastic rods with a robot-manipulated magnet for medical applications," *IEEE Transactions on Robotics*, vol. 33, no. 1, pp. 227–233, 2016.

[10] S. Zhang, M. Yin, Z. Lai, C. Huang, C. Wang, W. Shang, X. Wu, Y. Zhang, and T. Xu, "Design and characteristics of 3d magnetically steerable guidewire system for minimally invasive surgery," *IEEE Rob. and Auto. Letters*, vol. 7, no. 2, pp. 4040–4046, 2022.

[11] Z. Yang, L. Yang, M. Zhang, Q. Wang, S. C. H. Yu, and L. Zhang, "Magnetic control of a steerable guidewire under ultrasound guidance using mobile electromagnets," *IEEE Rob. and Auto. Letters*, vol. 6, no. 2, pp. 1280–1287, 2021.

[12] J. Edelmann, A. J. Petruska, and B. J. Nelson, "Magnetic control of continuum devices," *The International Journal of Robotics Research*, vol. 36, no. 1, pp. 68–85, 2017.

[13] S. Su, W. Yang, H. Dai, X. Xia, M. Lin, B. Sun, and C. Hu, "Investigation of the relationship between tracking accuracy and tracking distance of a novel

magnetic tracking system," *IEEE Sensors Journal*, vol. 17, no. 15, pp. 4928–4937, 2017.

[14] "Peripheral artery disease." `https://www.ucsfhealth.org/conditions/peripheral-artery-disease`. Accessed: September 20, 2023.

[15] "Angioplasty." `https://medlineplus.gov/angioplasty.html`. Accessed: September 20, 2023.

[16] "Peripheral artery angioplasty: Before your procedure." `https://myhealth.alberta.ca/Health/aftercareinformation/pages/conditions.aspx?hwid=ud2009`. Accessed: September 20, 2023.

[17] P. Schneider, *Endovascular skills: guidewire and catheter skills for endovascular surgery*. CRC press, 2019.

[18] S. Suzuki, S. Furui, H. Kohtake, N. Yokoyama, K. Kozuma, Y. Yamamoto, *et al.*, "Radiation exposure to patient's skin during percutaneous coronary intervention for various lesions, including chronic total occlusion," *Circulation Journal*, vol. 70, no. 1, pp. 44–48, 2006.

[19] L. S. Rosenthal, M. Mahesh, T. J. Beck, J. P. Saul, J. M. Miller, N. Kay, L. S. Klein, S. Huang, P. Gillette, E. Prystowsky, *et al.*, "Predictors of fluoroscopy time and estimated radiation exposure during radiofrequency catheter ablation procedures," *The American journal of cardiology*, vol. 82, no. 4, pp. 451–458, 1998.

[20] D. L. Miller, S. Balter, P. T. Noonan, and J. D. Georgia, "Minimizing radiation-induced skin injury in interventional radiology procedures," *Radiology*, vol. 225, no. 2, pp. 329–336, 2002.

[21] S. R. Walsh, C. Cousins, T. Y. Tang, M. E. Gaunt, and J. R. Boyle, "Ionizing radiation in endovascular interventions," *Journal of Endovascular Therapy*, vol. 15, no. 6, pp. 680–687, 2008.

[22] J. Coey, "Permanent magnet applications," *Journal of Magnetism and Magnetic Materials*, vol. 248, no. 3, pp. 441–456, 2002.

[23] P. Campbell, *Permanent Magnet Materials and their Application*. Cambridge University Press, 1996.

[24] "Dipolar halbach magnet stacks made from identically shaped permanent magnets for magnetic resonance," *Concepts in magnetic resonance.*, no. 4, 2010.

[25] Y. Kraftmakher, "Magnetic field of a dipole and the dipole–dipole interaction," *European Journal of Physics*, vol. 28, p. 409, mar 2007.

[26] T.-H. Chiang, Z.-H. Sun, H.-R. Shiu, K. C. Lin, and Y. Tseng, "Magnetic field-based localization in factories using neural network with robotic sampling," *IEEE Sensors J.*, vol. 20, no. 21, pp. 13110–13118, 2020.

[27] C. Hu, M. Q. Meng, and M. Mandal, "Efficient magnetic localization and orientation technique for capsule endoscopy," in *2005 IEEE/RSJ Int. Conf. on Intelligent Robots and Systems*, pp. 628–633, IEEE, 2005.

[28] S. Guitron, A. Guha, S. Li, and D. Rus, "Autonomous locomotion of a miniature, untethered origami robot using hall effect sensor-based magnetic localization," in *2017 IEEE International Conference on Robotics and Automation (ICRA)*, pp. 4807–4813, IEEE, 2017.

[29] D. Son, X. Dong, and M. Sitti, "A simultaneous calibration method for

magnetic robot localization and actuation systems," *IEEE Transactions on Robotics*, vol. 35, no. 2, pp. 343–352, 2018.

[30] C. Watson and T. K. Morimoto, "Permanent magnet-based localization for growing robots in medical applications," *IEEE Robotics and Automation Letters*, vol. 5, no. 2, pp. 2666–2673, 2020.

[31] C. C. Finlay, S. Maus, C. D. Beggan, T. N. Bondar, A. Chambodut, T. A. Chernova, A. Chulliat, V. P. Golovkov, B. Hamilton, M. Hamoudi, R. Holme, G. Hulot, W. Kuang, B. Langlais, V. Lesur, F. J. Lowes, H. Lühr, S. Macmillan, M. Mandea, S. McLean, C. Manoj, M. Menvielle, I. Michaelis, N. Olsen, J. Rauberg, M. Rother, T. J. Sabaka, A. Tangborn, L. Tøffner-Clausen, E. Thébault, A. W. P. Thomson, I. Wardinski, Z. Wei, and T. I. Zvereva, "International Geomagnetic Reference Field: the eleventh generation," *Geophysical Journal International*, vol. 183, pp. 1216–1230, 12 2010.

[32] C. Heunis, J. Sikorski, and S. Misra, "Flexible instruments for endovascular interventions: Improved magnetic steering, actuation, and image-guided surgical instruments," *IEEE robotics & automation magazine*, vol. 25, no. 3, pp. 71–82, 2018.

[33] C. Fischer, T. Quirin, C. Chautems, Q. Boehler, J. Pascal, and B. J. Nelson, "Gradiometer-based magnetic localization for medical tools," *IEEE Trans. on Magnetics*, 2022.

[34] C. Fischer, Q. Boehler, and B. J. Nelson, "Using magnetic fields to navigate and simultaneously localize catheters in endoluminal environments," *IEEE Rob. & Auto. Letters*, vol. 7, no. 3, pp. 7217–7223, 2022.

[35] J. D. Jackson, "Classical electrodynamics," 1999.

[36] C. R. Taylor, H. G. Abramson, and H. M. Herr, "Low-latency tracking of multiple permanent magnets," *IEEE Sensors Journal*, vol. 19, no. 23, pp. 11458–11468, 2019.

[37] J. Shawash and D. R. Selviah, "Real-time nonlinear parameter estimation using the levenberg–marquardt algorithm on field programmable gate arrays," *IEEE Trans. on Ind. Elec.*, vol. 60, no. 1, pp. 170–176, 2012.

[38] R. Lorbeer, A. Grotz, M. Dörr, H. Völzke, W. Lieb, J.-P. Kühn, and B. Mensel, "Reference values of vessel diameters, stenosis prevalence, and arterial variations of the lower limb arteries in a male population sample using contrast-enhanced mr angiography," *PloS one*, vol. 13, no. 6, p. e0197559, 2018.

[39] J. Wang, S. She, and S. Zhang, "An improved helmholtz coil and analysis of its magnetic field homogeneity," *Review of scientific instruments*, vol. 73, no. 5, pp. 2175–2179, 2002.